A&A 575, A119 (2015)
DOI: 10.1051/0004-6361/201424253

Astronomy & Astrophysics

The HARPS search for southern extra-solar planets

XXXVI. Planetary systems and stellar activity of the M dwarfs GJ 3293, GJ 3341, and GJ 3543⋆,⋆⋆

N. Astudillo-Defru[1,2], X. Bonfils[1,2], X. Delfosse[1,2], D. Ségransan[3], T. Forveille[1,2], F. Bouchy[3,4], M. Gillon[5], C. Lovis[3], M. Mayor[3], V. Neves[6], F. Pepe[3], C. Perrier[1,2], D. Queloz[3,7], P. Rojo[8], N. C. Santos[9,10], and S. Udry[3]

[1] Université Grenoble Alpes, IPAG, 38000 Grenoble, France
e-mail: nicola.astudillo@obs.ujf-grenoble.fr
[2] CNRS, IPAG, 38000 Grenoble, France
[3] Observatoire de Genève, Université de Genève, 51 ch. des Maillettes, 1290 Sauverny, Switzerland
[4] Laboratoire d'Astrophysique de Marseille, UMR 6110 CNRS, Université de Provence, 38 rue Frédéric Joliot-Curie, 13388 Marseille Cedex 13, France
[5] Institut d'Astrophysique et de Géophysique, Université de Liège, Allée du 6 Août 17, Bat. B5C, 4000 Liège, Belgium
[6] Departamento de Física, Universidade Federal do Rio Grande do Norte, 59072-970 Natal, RN, Brazil
[7] Cavendish Laboratory, J J Thomson Avenue, Cambridge, CB3 0HE, UK
[8] Departamento de Astronomía, Universidad de Chile, Camino El Observatorio 1515, Las Condes, Santiago, Chile
[9] Centro de Astrofísica, Universidade do Porto, Rua das Estrelas, 4150-762 Porto, Portugal
[10] Departamento de Física e Astronomia, Faculdade de Ciências, Universidade do Porto, Portugal

Received 22 May 2014 / Accepted 25 November 2014

ABSTRACT

Context. Planetary companions of a fixed mass induce reflex motions with a larger amplitude around lower-mass stars, which adds to making M dwarfs excellent targets for extra-solar planet searches. The most recent velocimeters with a stability of ∼1 m s^{-1} can detect very low-mass planets out to the habitable zone of these stars. Low-mass small planets are abundant around M dwarfs, and most of the known potentially habitable planets orbit one of these cool stars.
Aims. Our M-dwarf radial velocity monitoring with HARPS on the ESO 3.6 m telescope at La Silla observatory makes a major contribution to this sample.
Methods. We present here dense radial velocity (RV) time series for three M dwarfs observed over ∼five years: GJ 3293 (0.42 $M_{\odot}$), GJ 3341 (0.47 $M_{\odot}$), and GJ 3543 (0.45 $M_{\odot}$). We extracted these RVs through minimum χ^2-matching of each spectrum against a stack of all observed spectra for the same star that has a high signal-to-noise ratio. We then compared potential orbital signals against several stellar activity indicators to distinguish the Keplerian variations induced by planets from the spurious signals that result from rotational modulation of stellar surface inhomogeneities and from activity cycles.
Results. Two Neptune-mass planets – $m\sin(i) = 1.4 \pm 0.1$ and $1.3 \pm 0.1 M_{\rm nept}$ – orbit GJ 3293 with periods $P = 30.60 \pm 0.02$ d and $P = 123.98 \pm 0.38$ d, possibly together with a super-Earth – $m\sin(i) \sim 7.9 \pm 1.4\ M_{\oplus}$ – with period $P = 48.14 \pm 0.12$ d. A super-Earth – $m\sin(i) \sim 6.1\ M_{\oplus}$ – orbits GJ 3341 with $P = 14.207 \pm 0.007$ d. The RV variations of GJ 3543, on the other hand, reflect its stellar activity rather than planetary signals.

Key words. techniques: radial velocities – stars: late-type – stars: individual: GJ 3293 – stars: individual: GJ 3341 – stars: individual: GJ 3543 – planetary systems

1. Introduction

A planet of a given mass induces a stronger reflex motion on a less massive host star. Around the low-mass M dwarfs, present-day observing facilities can consequently detect planets that are only a few times more massive than Earth (Fressin et al. 2013; Mayor et al. 2009). These very low-mass stars dominate Galactic populations by approximately 3 to 1 (e.g., van Dokkum & Conroy 2010), and most of them host planets: Bonfils et al. (2013a) estimated that $0.88^{+0.55}_{-0.19}$ planets orbit each early- to mid-M dwarf with a period shorter than 100 days, while Dressing & Charbonneau (2013) found that each star with effective temperatures below 4000 K is orbited by $0.90^{+0.04}_{-0.03}$ planets with radii between 0.5 and 4 $R_{\oplus}$ and an orbital period shorter than 50 days. Their high Galactic abundance combined with their abundant planets make M dwarfs excellent targets for planet searches. These stars consequently are the focus of several ongoing surveys – with both radial velocity (RV; e.g., HARPS; Bonfils et al. 2013a) and transit techniques (e.g. MEarth; Nutzman & Charbonneau 2008). Several instruments are being developed to specifically target these stars, such as SPIRou (Delfosse et al. 2013b), CARMENES (Quirrenbach et al. 2012), NGTS (Wheatley et al. 2013), and Exoplanets in

⋆ Based on observations made with the HARPS instrument on the ESO 3.6 m telescope under the program IDs 072.C-0488, 082.C-0718 and 183.C-0437 at Cerro La Silla (Chile).

⋆⋆ Tables A.1–A.3 (radial velocity data) are available in electronic form at http://www.aanda.org and at the CDS via anonymous ftp to cdsarc.u-strasbg.fr (130.79.128.5) or via http://cdsarc.u-strasbg.fr/viz-bin/qcat?J/A+A/575/A119

Transit and their Atmosphere (ExTrA; Bonfils et al., in prep.), mostly in the near-infrared spectral range where M dwarfs are brighter and where a given photon noise can thus be achieved within a much shorter integration time.

Much interest is currently focused on discovering broadly Earth-like planets that orbit within the habitable zone (HZ) of their host star. The HZ zone, by definition, is the range of host star distances for which the incident stellar flux allows water on a planetary surface to remain in the liquid phase, and after accounting for greenhouse effects, it corresponds to a surface equilibrium temperature of between 175 K and 270 K (Selsis et al. 2007). That zone is much closer in for a low-luminosity M dwarf than for a brighter solar-type star: the orbital period for a HZ planet ranges from a week to a few months across the M dwarf spectral class, compared to one year for the Sun-Earth system. This relaxes the $\sim$10 cm s^{-1} precision required to detect an Earth-equivalent orbiting a Sun-equivalent to $\sim$1 m s^{-1} for the same planet orbiting in the habitable zone of an M dwarf. Characterizing that planet during transit, if any occurs, is furthermore facilitated considerably by the much higher planet-to-stellar surface ratio. The equilibrium surface temperature of a planet secondarily depends on the nature of its atmosphere, making planetary mass an important parameter as well. Bodies with $M < 0.5\ M_\oplus$ are expected to retain atmospheres that are too shallow for any water to be liquid, while planets with $M > 10\ M_\oplus$ are expected to accrete a very thick atmosphere mainly dominated by hydrogen and helium (Selsis et al. 2007). These considerations together make GJ 667Cc (Delfosse et al. 2013a; Bonfils et al. 2013a), GJ 163 (Bonfils et al. 2013b), and Kepler-186f (Quintana et al. 2014) some of the best current candidates for potentially habitable planets.

Stellar activity affects habitability (e.g., Vidotto et al. 2013), but more immediately, it can induce false-positives in planet detection. M dwarfs remain active for longer than more massive stars because they do not dissipate their angular momentum as fast as their more massive brethren, and stellar activity correlates strongly with rotation period (Noyes et al. 1984). Additionally, lower mass stars are more active for a fixed rotation period (Kiraga & Stepien 2007). Activity, in turn, affects measured stellar velocities through a number of mechanisms: stellar spots deform spectral lines according to their position on the stellar surface, the up-flowing and down-flowing regions of convective cells introduce blue- and red-shifted components to the line shapes, and stellar oscillations also introduce a RV jitter. Stellar activity diagnostics are therefore essential to filter out spurious radial velocity signals that can otherwise be confused with planets (Bonfils et al. 2007).

Cross-correlation with either an analog or a numerical mask is widely used to extract radial velocities from spectra (Baranne et al. 1996). This technique concentrates the information of all the lines in the mask into an average line with a very high signal-to-noise ratio (S/N). It therefore enables characterizing the line profile in great detail. In addition to the usually minor effect of telluric absorption lines, any variation of the full-width at half-maximum (FWHM), contrast, or bisector-span of the cross-correlation functions that correlate with the radial velocity variations denotes that they originate in stellar phenomena such as spots, visible granulation density, or oscillations (Queloz et al. 2001; Boisse et al. 2011; Dumusque et al. 2011). Plages or filaments on the stellar surface can additionally be detected through emission in the Ca II H&K, and Hα lines, for example (Gomes da Silva et al. 2011).

Here we present analyses of GJ 3293 and GJ 3341 for which our HARPS measurements indicate the presence of planets, and for GJ 3543, for which we conclude that stellar activity more likely explains the RV variations. Section 2 briefly describes the observations and reduction process, Sect. 3 discusses the properties of each star in some detail, while Sects. 4–6 describe the RVs analysis and orbital solutions and examine stellar activity. Finally, we conclude in Sect. 7.

2. Spectra and Doppler analysis from HARPS

The High Accuracy Radial velocity Planets Searcher (HARPS) is a fiber-fed, cross-dispersed echelle spectrograph installed on the 3.6 m telescope at La Silla observatory in Chile. The instrument diffracts the light over two CCDs, where 72 orders cover the 380 to 630 nm spectral range with a resolving power of 115 000 (Mayor et al. 2003). HARPS stands out by its long-term stability, ensured by a vacuum enclosure and a temperature-stabilized environment. To achieve sub-m/s precision, the spectrograph produces spectra for light injected through two fibers. One receives light from the target star, the other can be simultaneously (or not) illuminated with a calibration reference to correct instrumental drifts during the observations.

The HARPS pipeline (Lovis & Pepe 2007) automatically reduces the data using nightly calibrations and measures the radial velocity by cross-correlation with a binary mask (Pepe et al. 2002) that depends on the spectral type. The numerical mask for M dwarfs consists of almost 10 000 holes, placed on spectral lines selected for their large amount of Doppler information. The whole procedure is complete shortly after the end of each exposure.

The visual band spectra of the coolest stars contain very many overlapping molecular features with essentially no continua. Under these circumstances, a binary mask makes suboptimal use of the available Doppler information. In this study, we therefore recomputed RVs from the order-by-order spectra extracted by the HARPS pipeline. For each target, we used the RVs measured by the HARPS pipeline for the individual spectra together with the corresponding barycentric correction to align all spectra to the frame of the solar system barycenter. This aligns the stellar lines, while the telluric features are shifted by minus the barycentric velocity of each epoch. We then computed the median of these spectra to produce a high S/N template spectrum for each target. At that stage, we produced a template of the telluric absorption spectrum by computing the median of the residuals (aligned in the laboratory reference frame) of subtracting the high S/N template from the individual spectra. We then used this telluric spectrum to produce an improved stellar template by constructing it again without the now known telluric lines. This process can be iterated in principle, but we found that it effectively converges after the first iteration. Finally, we measured new radial velocities by minimizing the χ^2 of the residuals between the observed spectra and shifted versions of the stellar template, with all spectral elements contaminated by telluric lines masked out (e.g., Howarth et al. 1997; Zucker & Mazeh 2006, Astudillo-Defru et al., in prep.). Astudillo-Defru et al. (in prep.) will provide a detailed description of the algorithm implementation and will characterize its performance.

Our observation strategy is described in detail in Bonfils et al. (2013a) and is only summarized for convenience here. We chose to observe without illuminating the reference fiber because we only targeted a $\sim$1 m s^{-1} precision; this choice provides clean observations of the Ca II H&K lines for later stellar activity analysis, which is particularly important for M dwarfs. We hence made use of wavelength calibrations acquired before the beginning of the night. The exposure time was 900 s for all frames.

Table 1. Stellar properties of the three targets.

	GJ 3293	GJ 3341	GJ 3543
Spectral type	M2.5	M2.5	M1.5
α (J2000)	$04^h28^m35.6^s$	$05^h15^m46.7^s$	$09^h16^m20.7^s$
δ (J2000)	$-25°10'16''$	$-31°17'46''$	$-18°37'33''$
V[(1)]	11.962	12.080	10.739
J[(2)]	8.362 ± 0.024	8.592 ± 0.020	7.351 ± 0.021
H[(2)]	7.749 ± 0.038	7.990 ± 0.049	6.759 ± 0.047
K[(2)]	7.486 ± 0.033	7.733 ± 0.023	6.492 ± 0.024
π [mas][(3,4,3)]	55 ± 9	43.18 ± 1.40	80 ± 15
M_V	10.66 ± 0.31	10.26 ± 0.07	10.25 ± 0.34
M_K	6.19 ± 0.31	5.91 ± 0.07	6.01 ± 0.34
BC_K	2.71 ± 0.08	2.68 ± 0.06	2.68 ± 0.06
L [$L_{\rm Sun}$][(6)]	0.022	0.029	0.026
M [$M_\odot$][(5)]	0.42	0.47	0.45
R [$R_\odot$][(7)]	0.404 ± 0.027	0.439 ± 0.027	0.432 ± 0.027
$T_{\rm eff}$ [K][(7)]	3466 ± 49	3526 ± 49	3524 ± 49
Fe/H[(8)]	0.02 ± 0.09	−0.09 ± 0.09	−0.13 ± 0.09
μ_α [mas/yr][(9)]	−87 ± 5	504 ± 5	−314.6 ± 3.4
μ_δ [mas/yr][(9)]	−475 ± 5	243 ± 5	148.0 ± 3.3
dv_r/dt [m/s/yr][(10)]	0.097 ± 0.018	0.167 ± 0.008	0.035 ± 0.007
$HZ_{\rm In}$ [AU][(11)]	0.112	0.129	0.124
$HZ_{\rm Out}$ [AU][(11)]	0.305	0.350	0.335

References. (1) Zacharias et al. (2012); (2) Cutri et al. (2003); (3) Gliese & Jahreiß (1991); (4) Riedel et al. (2010); from (5) Delfosse et al. (2000); (6) Leggett et al. (2001); (7) Boyajian et al. (2012) and (8) Neves et al. (2014) relationships; (9) Salim & Gould (2003); (10) Kürster et al. (2003); (11) Selsis et al. (2007).

This is adequate for a 0.80 m s^{-1} precision for visual magnitudes between 7 and 10, but the velocities of the fainter stars we discuss here have significantly higher photon noise errors.

3. Stellar properties of GJ 3293, GJ 3341, and GJ 3543

GJ 3293 (LHS 1672), GJ 3341 (LHS 1748), and GJ 3543 (L 749-34) are high proper motion early-M dwarfs (M2.5, M2.5, and M1.5, respectively). We used the BC_K bolometric correction of Leggett et al. (2001) and the photometric distance of Gliese & Jahreiß (1991) to compute their luminosity. We also estimated the effective temperature ($T_{\rm eff}$), stellar radius, and luminosity from the $V-K$ color and metallicity relationship of Boyajian et al. (2012); the two luminosities agree well for the three targets. We derived the stellar metallicities – and $T_{\rm eff}$, for comparison – from our spectra using the methods of Neves et al. (2014); the two determinations of $T_{\rm eff}$ agree to better than their error bars for all three stars, and we only quote the Boyajian et al. (2012) value. The masses were computed using the Delfosse et al. (2000) K-band mass versus absolute magnitude relation. We calculated the UVW space motions with the Johnson & Soderblom (1987) orientation convention, and assigned kinematic populations following Leggett (1992). We used the proper motion and distance to compute the secular radial acceleration dv/dt (Kürster et al. 2003), from which we corrected the radial velocities. Following Selsis et al. (2007), we adopted recent Venus and early Mars criteria for the inner ($HZ_{\rm In}$) and outer ($HZ_{\rm Out}$) edges of the habitable zone. Table 1 summarizes the properties of the three targets.

GJ 3293 is located in the Eridanus constellation and is 18.2 ± 2.6 pc (Gliese & Jahreiß 1991) away from the Sun. Its Galactic velocity parameters, $U = -27.3 \pm 17.1$ km s^{-1}, $V = -25.9 \pm 6.6$ km s^{-1}, and $W = -22.2 \pm 23.1$ km s^{-1}, leave its kinematic population uncertain in part because of the large uncertainty on its photometric distance; GJ 3293 could belong either to the young or the young-old disk population. Its metallicity ([Fe/H] = 0.02) is close to solar and suggests that it is part of the young disk, but is consistent with either option.

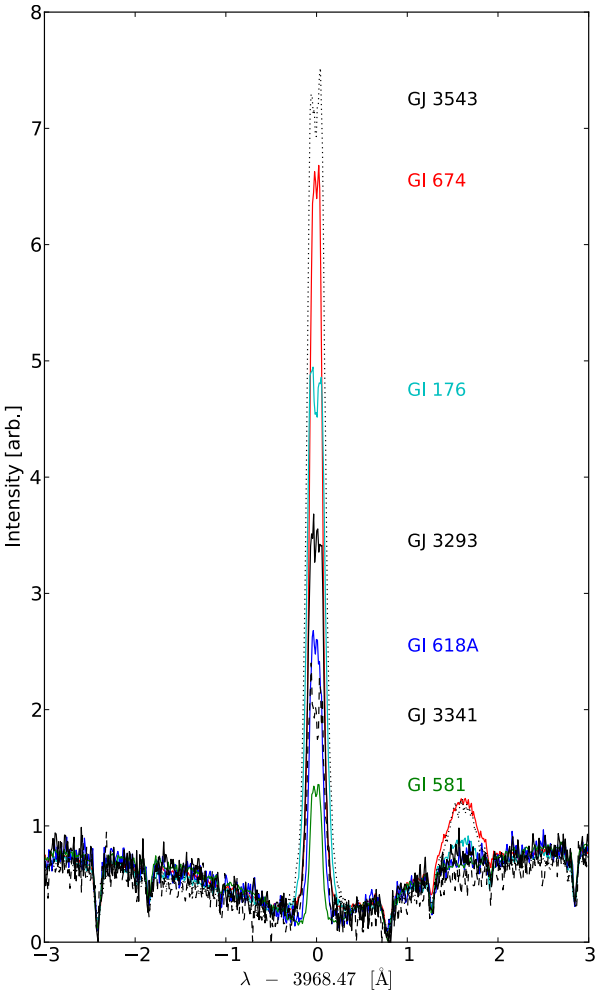

Fig. 1. Median spectra centered on the Ca II H line for reference stars, sorted by increasing rotation period: Gl 674 (red line, M3, $P_{\rm rot}$ = 35 d), Gl 176 (cyan line, M2.5, $P_{\rm rot}$ = 39 d), Gl 618A (blue line, M3, $P_{\rm rot}$ = 57 d), and Gl 581 (green line, M2.5, $P_{\rm rot}$ = 130 d). Median spectra for the targets of this paper, with no a priori known rotation period: GJ 3543 (black dotted line, M1.5), GJ 3293 (black full line, M2.5), and GJ 3341 (black dashed line, M2.5).

GJ 3341 is located in the Columba constellation at a distance of 23.2 ± 0.7 pc (Riedel et al. 2010). Its proper motion, distance, and systemic velocity ($\gamma = 47.803 \pm 0.003$) result in $U = 52.5 \pm 0.6$ km s^{-1}, $V = -52.0 \pm 0.8$ km s^{-1}, and $W = 24.4 \pm 3.2$ km s^{-1}. This formally makes GJ 3341 a young-old disk member.

GJ 3543 is located in the Hydra constellation and at 12.5 ± 2.0 pc from the Sun (Gliese & Jahreiß 1991). Its space motion components $U = 23.8 \pm 11.3$ km s^{-1}, $V = -9.0 \pm 2.0$ km s^{-1}, and $W = -2.7 \pm 1.7$ km s^{-1} place GJ 3543 in the young-disk box, while its metallicity ([Fe/H] = −0.13) is somewhat low for the Galactic young disk.

4. Radial velocities of GJ 3293

The 145 RV measurements of GJ 3293 span 1514 d. Their σ_e = 7.69 m s^{-1} dispersion is much higher than the average Doppler

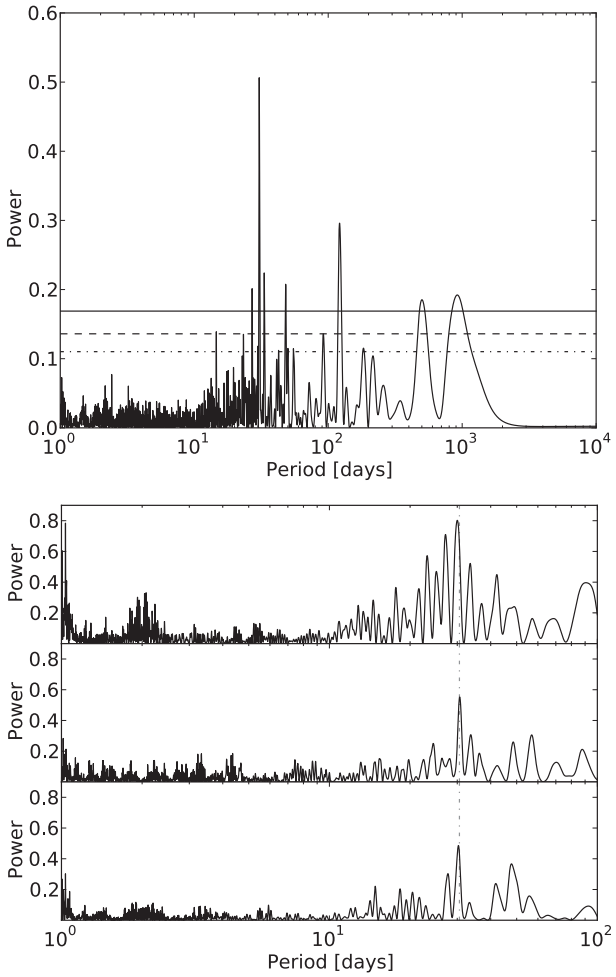

Fig. 2. *Top panel*: periodogram of the GJ 3293 RVs. The solid line, dashed line, and dashed dotted line represent the 0.3%, 4.6%, and 31.7% FAP levels, corresponding to 3σ, 2σ, and 1σ confidence, respectively. *Bottom panel*: periodograms for epochs 2008−2009 (34 measurements, first row), 2010−2011 (52 measurements, second row), and 2012−2013 (59 measurements, third row); the stability of the 30 d signal (dash-dotted vertical) is clear.

uncertainty $\langle\sigma_i\rangle = 1.76\,\mathrm{m\,s^{-1}}$, which represents the weighted arithmetic mean of the estimated photon noise (Bouchy et al. 2001) and instrumental errors. Both an F-test with $F = \sigma_e^2/\langle\sigma_i\rangle^2$ and a χ^2 test for a constant model given $\langle\sigma_i\rangle$ returned negligible probabilities ($<10^{-9}$) that the photon noise combined with wavelength calibration and guiding uncertainties explains the measured dispersion.

We thus searched for periodicity with floating-mean periodograms, with a periodogram-normalization choice where 1 stands for a perfect fit of a sine wave to the data, and 0 points to no improvement over a constant model (Zechmeister & Kürster 2009). In addition to the commonly used 1% false-alarm probability (FAP) confidence level, we plot values covering 68.3%, 95.4%, and 99.7% of the periodogram power distributions, equivalent to 1σ (31.7% FAP), 2σ (4.6% FAP), and 3σ confidences (0.3% FAP).

Figure 2 shows the periodogram of the GJ 3293 time series and reveals a clear power excess around $P = 30.6$ d, with $p_{\max} = 0.51$. Additional peaks above the 0.3% FAP ($p = 0.17$) appear at 121.6, 33.3, 48.2, 27.1, 919.5, and 500.9 d, with powers of 0.30, 0.22, 0.21, 0.20, 0.19, and 0.19, respectively. To further evaluate the confidence on the $P = 30.6$ d signal given our measurement errors and sampling, we generated 1000 synthetic datasets by rearranging the radial velocities and holding the dates fixed. None of the periodograms generated for these bootstrapped datasets had maximum power above 0.3. The FAP on the 30.6 d signal, with 0.51 power, is therefore well below 1/1000. The prescription of Horne & Baliunas (1986) for the periodogram interpretation gives FAP(30.6 d) $= 2.8 \times 10^{-19}$, and the 30.6 d peak is well above any of the considered confidence levels.

Table 2. One-Keplerian fit for GJ 3293.

	GJ 3293b
P [d]	30.57 ± 0.02
T_0 [JD–2 400 000]	55661.6 ± 2.3
ω [deg]	169.4 ± 26.7
e	0.16 ± 0.08
K_1 [m s^{-1}]	8.9 ± 0.8
$m\sin(i)$ [$M_{\rm nept}$]	1.4 ± 0.1
a [AU]	0.1433
$N_{\rm meas}$	145
Span [d]	1514
$\langle\sigma_i\rangle$ [m s^{-1}]	1.76
σ_e [m s^{-1}]	5.34
χ^2_ν	9.28

We used *yorbit* (Ségransan et al., in prep.) to adjust Keplerian orbits with an MCMC algorithm. Without any prior on the orbit, this converged on a solution with period $P = 30.565 \pm 0.024$ d, eccentricity $e = 0.158 \pm 0.082$, and semi-amplitude $K_1 = 8.87 \pm 0.83\,\mathrm{m\,s^{-1}}$. This solution reduces the rms dispersion of the residuals to $\sigma_e = 5.34\,\mathrm{m\,s^{-1}}$ and the reduced χ^2 to $\chi^2_\nu = 9.28 \pm 0.37$. Given an $M = 0.42\ M_\odot$ stellar mass (with 10% uncertainty), the minimum mass for the planet is $m\sin(i) = 1.4 \pm 0.1 M_{\rm nept}$. Table 2 summarizes the orbital and derived parameters. The ratio of the eccentricity (e) to its uncertainty (σ_e) is $e/\sigma_e < 2.49$, and therefore is below the usual thresholds for significant eccentricity[1] (Lucy 2013). We adopted the eccentricity that *yorbit* converged on when analyzing the residuals for additional signals, but its low value makes that choice unimportant.

Many of the peaks in the top panel of Fig. 2 have no counterpart in the periodogram of the subtraction residuals of the 30.6 d signal (Fig. 3) and therefore represent no more than aliases of that signal. A peak around 123.4 d dominates this periodogram of the residuals, with $p_{\max} = 0.64$. A bootstrap test with one thousand (1000) iterations produced no signal above 0.3, and the FAP of the dominant peak is therefore well under 10^{-3}. The prescription of Horne & Baliunas (1986) evaluates the FAP to 3.3×10^{-29} for the 123.4 d peak. Other peaks above a 0.3% FAP ($p = 0.17$) occur at periods 92.1, 48.2, 218.8, 186.5, 517.2, 55.0, and 41.2 d, and with powers of 0.39, 0.33, 0.27, 0.24, 0.24, 0.22, and 0.19. None of them is sufficiently strong that confusing the 123.4 d signal for one of its aliases would be a problem. We used *yorbit* to model the RVs with two Keplerian signals, again with no prior on the orbital parameters. The parameters of the first Keplerian are essentially unchanged from the one-Keplerian fit, and the second has a period $P = 123.76 \pm 0.30$ d, eccentricity $e = 0.331 \pm 0.057$, and semi-amplitude $K_1 = 6.430 \pm 0.423\,\mathrm{m\,s^{-1}}$, which correspond to a minimum planetary mass of $m\sin(i) = 1.5 \pm 0.1 M_{\rm nept}$.

[1] $\varepsilon_{95}/\mu = 3.34$ for the eccentricity upper limit, where $\mu = \sigma_e$ and $\alpha(\%) = 5$ for the detection threshold – using the nomenclature of Lucy (2013).

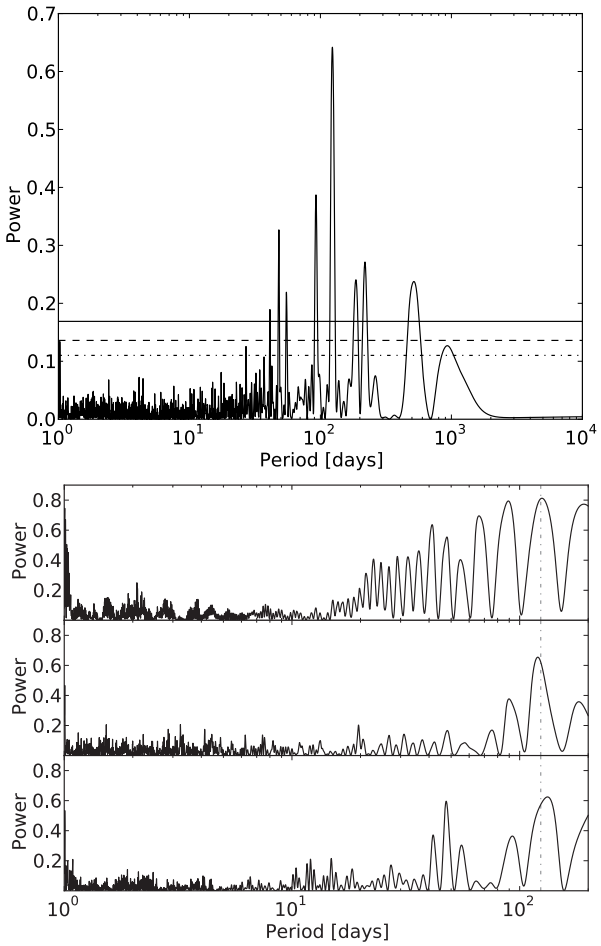

Fig. 3. *Top panel*: periodogram of the residuals from subtracting the first Keplerian (P = 30.6 d). The horizontal lines have the same meaning as in Fig. 2. *Bottom panel*: we split for subsets of the observational epochs, defined in the caption of Fig. 2, and performed their peridogram; in spite of the poor sampling of some of the subsets for a 123 d period, all show a peak around this period.

Table 3. Fit for two-Keplerian orbits for GJ 3293.

	GJ 3293b	GJ 3293c
P [d]	30.60 ± 0.01	123.75 ± 0.30
T_0 [JD–2 400 000]	55 638.7 ± 2.6	55 687.8 ± 3.8
ω [deg]	−103.0 ± 31.3	−21.4 ± 14.2
e	0.07 ± 0.04	0.33 ± 0.06
K_1 [m s^{-1}]	9.6 ± 0.4	6.4 ± 0.4
$m \sin(i)$ [$M_{\rm nept}$]	1.5 ± 0.1	1.5 ± 0.1
a [AU]	0.1434	0.3640
$N_{\rm meas}$	145	
Span [d]	1514	
$\langle\sigma_i\rangle$ [m s^{-1}]	1.76	
$\sigma_{\rm e}$ [m s^{-1}]	2.86	
χ^2_ν	2.76	

Table 3 summarizes the parameters of the two Keplerians. The dispersion and the reduced χ^2 decrease to $\sigma_{\rm e}$ = 2.86 m s^{-1} and χ^2_ν = 2.76 ± 0.20. An F-test of this new $\sigma^2_{\rm e}$ against the average internal errors $\langle\sigma_i\rangle^2$ and a χ^2 against a constant model return $P(F) = 5.7 \times 10^{-9}$ and $P(\chi^2) < 10^{-9}$, which means that significant dispersion remains above the internal errors.

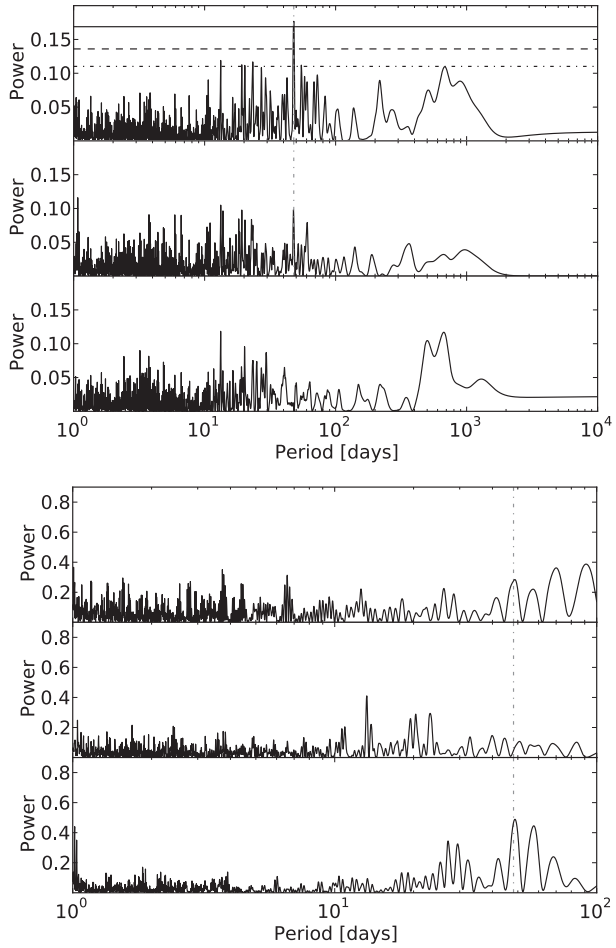

Fig. 4. *Top panel*. *First row*: periodogram of the subtraction residuals of two Keplerians with periods of 30.6 and 123.6 d, dominated by a 48 d peak. The horizontal lines represent FAP levels, as described in the captions of Fig. 2. *Second row*: periodogram of the residuals after subtracting three Keplerians with periods of 30.6, 123.6, and 439 d. The vertical dash-dotted line marks a P = 48 d period. *Third row*: periodogram of the residuals after subtracting Keplerians with periods of 30.6, 123.6, and 48 d. *Bottom panel*: periodogram of the residuals after subtracting the 30.6 and 123.6 d signals for each subset of epochs described in the captions of Fig. 2. The 48 d signal is not seen for the 2010−2011 observational epochs, which have a poor sensitivity to that period range because their sampling incidentally concentrates around just two phases.

A single peak dominates the periodogram of the subtraction residuals of the two Keplerians (Fig. 4), implying that the other strong peaks in Figs. 2 and 3 are aliases of the 30.6 and 123.8 d signals. This peak at 48 d has power $p_{\rm max}$ = 0.18, which corresponds to a 0.15% FAP (p = 0.15 corresponds to a 1% FAP and p = 0.17 to a 3σ confidence level). An unconstrained search for a three-Keplerian solution with *yorbit* converged on the two Keplerians described above plus a highly eccentric (e = 0.925 ± 0.022) Keplerian with a period of 439 d. The third orbit crosses the other two, making the solution almost certainly unstable on very short time scales, and therefore unphysical. Spurious highly eccentric orbits are favored when noise becomes significant and/or sampling is poor, with the highest velocity excursions typically found at the most poorly sampled phases of the orbit. The periodogram of the residuals of that unphysical solution still has a 48 d peak, but with much reduced power (p = 0.10, 0.63 FAP, middle panel of Fig. 4). This indicates that our sampling couples signals at periods of

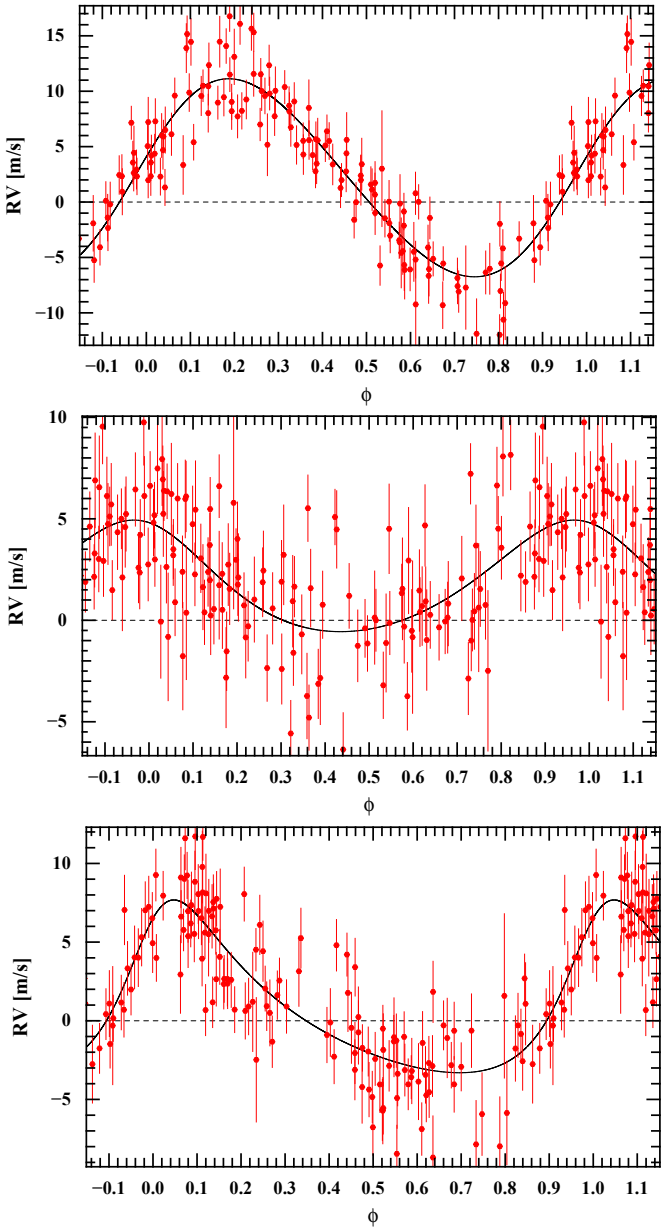

Fig. 5. Radial velocities phased for each signal. P = 30.59 d *top panel*, P = 48.07 d *middle panel*, and P = 123.79 d *bottom panel*.

48 and 439 d, but incompletely. We therefore constrained the period of the third Keplerian to the [2, 100] d range to avoid convergence on the spurious longer period eccentric solution. This converged on a Keplerian with $P = 48.072 \pm 0.120$ d, $e = 0.190 \pm 0.134$, and $K_1 = 2.515 \pm 0.393\,\mathrm{m\,s^{-1}}$, which corresponds to a minimum mass of $m\sin(i) = 7.9 \pm 1.4\ M_\oplus$, plus the two Keplerians with periods of 30.6 and 123.4 d. Following Lucy (2013), $e_b/\mu < 2.49$ and the eccentricity therefore remains below the detection threshold. Figure 5 shows the Keplerian solution. The dispersion is $\sigma_e = 2.45\,\mathrm{m\,s^{-1}}$ and the reduced χ^2 is $\chi^2_\nu = 2.11 \pm 0.18$. An F-test of this σ_e^2 against $\langle\sigma_i\rangle^2$ yields a $P(F) = 4.3 \times 10^{-5}$ probability that this would occur by chance. The RVs therefore vary by significantly more than expected from their known measurement errors. Possible explanations include additional companions, stellar activity, or a non-Gaussian or underestimated noise. The periodogram of the residuals of the three-Keplerian solution (bottom panel of Fig. 4 has no peak above a 12% FAP (11.8% at 13.3 d and 11.7% at 669.6 d). Our final solution (Table 4) additionally includes a quadratic drift, which improves the residuals by a formally significant amount and suggests a possible component at a wider separation.

Table 4. Fit for three-Keplerian orbits plus a quadratic drift for GJ 3293.

	GJ 3293b	GJ 3293(c)	GJ 3293d
P [d]	30.60 ± 0.02	48.14 ± 0.12	123.98 ± 0.38
T_0 [JD–2 400 000]	55 640.3 ± 1.9	55 643.3 ± 6.0	55 684.9 ± 3.7
ω [deg]	−77.7 ± 24.2	17.3 ± 46.3	−38.0 ± 14.1
e	0.09 ± 0.04	0.16 ± 0.13	0.37 ± 0.06
K_1 [m s^{-1}]	8.9 ± 0.4	2.7 ± 0.4	5.5 ± 0.4
$m\sin(i)$ [$M_{\rm nept}$]	1.4 ± 0.1	0.5 ± 0.1	1.3 ± 0.1
a [AU]	0.1434	0.1939	0.3644
γ [km s^{-1}]	13.297 ± 0.018		
$\dot\gamma$ [m s^{-1} yr^{-1}]	−0.103 ± 0.002		
$\ddot\gamma$ [m s^{-1} yr^{-2}]	0.325 ± 0.001		
$N_{\rm meas}$	145		
Span [d]	1514		
$\langle\sigma_i\rangle$ [m s^{-1}]	1.76		
σ_e [m s^{-1}]	2.41		
χ^2_ν	2.07		

4.1. Stellar activity

We computed periodograms for the FWHM, bisector span, and contrast of the cross-correlation function (CCF), as well as for the S and Hα indices, to investigate whether some of the periodicities can be attributed to stellar activity. We also searched for correlations between these activity indicators and the radial velocities and their residuals after subtracting subsets of the Keplerian orbits.

The periodograms of the bisector span, FWHM, contrast, and S-index show no dominant peaks, while that for Hα shows one peak at over 3σ confidence at 41 d (Fig. 6 top); since the strength of the Ca II emission in GJ 3293 is intermediate between those for Gl 176 (P = 39 d) and Gl 618A (P = 57 d) – Fig. 1, this peak may reflect the stellar rotation period. We see no correlation between any of the activity indicators and either the radial velocities or the residuals from subtracting the Keplerian orbits (Fig. 6, bottom, for Hα).

To evaluate the stability of the 30.6, 48.1 and 123.8 d signals over time, we split the RVs into three groups of epochs: 2008−2009 (34 measurements), 2010−2011 (52 measurements), and 2012−2013 (59 measurements). We computed periodograms of the RVs and of their residuals after successively subtracting the stronger Keplerians. These seasonal periodograms consistently show strong evidence for the 30.6 and 123.8 d signals. The weaker 48.1 d signal is detected in the 2008−2009 and 2012−2013 periodograms, but not in the 2010−2011 epochs (bottom panels of Figs. 2–4). After investigating, we realized that the 2010−2011 measurements are strongly clustered at just two phases for a 48.1 d period and therefore highly insensitive to that signal. There is consequently strong evidence for the stability and planetary nature of the 30.6 and 123.8 d signal, but somewhat weaker evidence for the 48.1 d signal. The unfortunate phasing of the 2010−2011 measurements and the weaker signal do not allow strong limits against a possibly time-varying amplitude. While the period of that signal is moderately close to the 41 d possible stellar rotation and its true nature thus remains somewhat uncertain, the lack of any

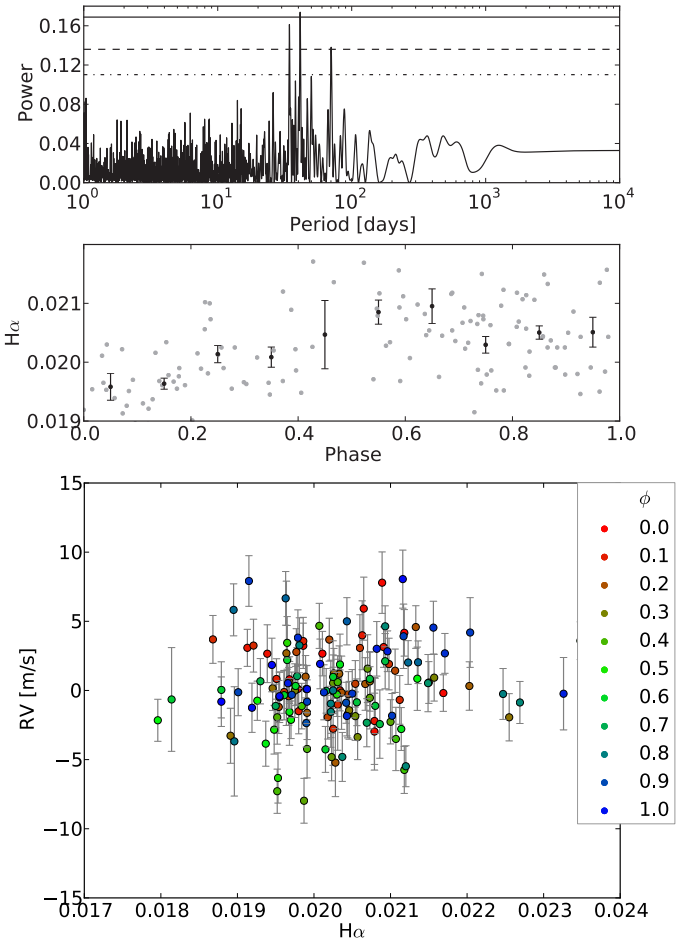

Fig. 6. *Top*: periodogram of the Hα emission index of GJ 3293, with a peak above the 3σ confidence level at 41 d and two peaks the above 2σ confidence level at 34 and 70 d. *Middle*: the Hα index phased to P = 41 d (gray dots); the black dots are binned by 0.1 in phase. *Bottom*: RVs corrected for the 30.6 and 123.8 d signals against the Hα-index; the colors represent the phase of the 48 d signal from Table 4 (as represented in the middle panel of Fig. 5).

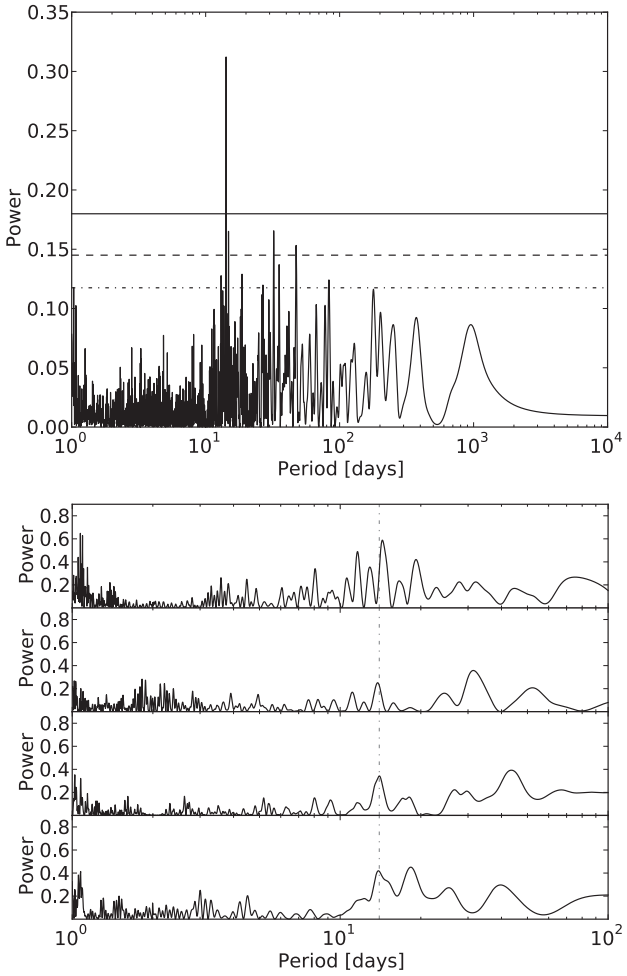

Fig. 7. *Top panel*: periodogram of the GJ 3341 radial velocities, with a peak above the 3σ confidence limit at 14 d (continuous black line). *Bottom panel*: periodograms for four subsets of epochs (BJD–2 400 000 = 54 800–55 000, 55 400–55 600, 55 800–56 050, 56 150–56 300); the 14 d (vertical dash-dotted line) peak is always present.

significant correlation between radial velocity and the stellar activity indicators suggest that it is planetary.

5. Radial velocities of GJ 3341

We obtained 135 RV measurements of GJ 3341, spanning 1456 d. Their dispersion is σ_e = 3.51 m s^{-1}, while the combined photon noise and instrumental errors average to $\langle\sigma_i\rangle$ = 1.89 m s^{-1}. An F-test and a χ^2 comparison against a constant model yield probabilities $P(F)$ and $P(\chi^2) < 10^{-9}$ that the RV dispersion is explained by the RVs uncertainties. The periodogram (Fig. 7) shows a peak at 14.21 d with power of p = 0.31. 1000 iterations of bootstrap randomization produced no random data set with a power above 0.24, and the FAP for this peak is therefore well below 10^{-3}. The Horne & Baliunas (1986) recipe results in an FAP of 2.73×10^{-8}.

A Keplerian fit with *yorbit* converges on an orbit with period P = 14.207 ± 0.007 d, eccentricity e = 0.31 ± 0.11, and semi-amplitude K_1 = 3.036 ± 0.408. Given the stellar mass of M = 0.47 $M_\odot$, the corresponding minimum planetary mass is 6.6 ± 0.1 $M_\oplus$. Table 5 summarizes the solution parameters. This solution (Fig. 8) has a reduced χ^2 of χ^2 = 2.28 ± 0.19 and a σ_e = 2.86 m s^{-1} dispersion of the residuals. An F-test and a χ^2 test for a constant model resulted in probabilities $P(F) = 1.18 \times 10^{-6}$ and $P(\chi^2) < 10^{-9}$ that this dispersion is explained by photon noise combined with instrumental errors. The periodogram of the residuals shows a p = 0.18 peak at 41 d, above the p = 0.16 level for a 1% FAP and grazing the 3σ confidence level. We were unable to reliably fit a Keplerian to these

Table 5. One-Keplerian fit for GJ 3341.

	GJ 3341b
P [d]	14.207 ± 0.007
T_0 [JD–2 400 000]	55 622.7 ± 0.8
ω [deg]	42.32 ± 4.3
e	0.31 ± 0.11
K_1 [m s^{-1}]	3.04 ± 0.41
$m \sin(i)$ [$M_\oplus$]	6.6 ± 0.1
a [AU]	0.089
γ [km s^{-1}]	47.803 ± 0.003
N_{meas}	135
Span [d]	1455.9
$\langle\sigma_i\rangle$ [m s^{-1}]	1.89
σ_e [m s^{-1}]	2.86
χ^2_ν	2.28

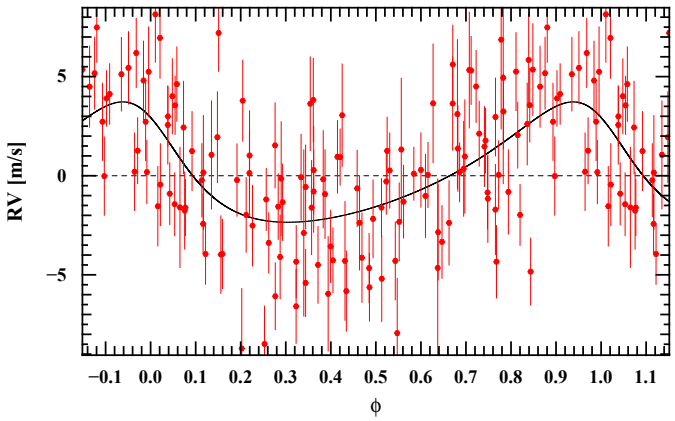

Fig. 8. GJ 3341 radial velocities phased for a 14.2 d period.

residuals, and stellar activity is therefore a more likely explanation for this additional RV variability.

5.1. Stellar activity

The periodogram of the Hα (Fig. 9) and S indices, contrast, bisector-span, and FWHM of the CCF show no evidence of stellar activity which could explain the RVs variations, and nor do plots of the RV as a function of these parameters. Subtracting a long-term trend visible in Hα index, however, increases the power in a pre-existing 46 d peak of its periodogram (Fig. 9) to 0.24, above the 3σ confidence level. Phasing the Hα index with this period produces relatively smooth and approximately sinusoidal variations, compatible with the signature of stellar rotation. This period is somewhat shorter than expected from the relatively weak Ca II emission of GJ 3341, which is intermediate in strength between those of Gl 618A (P = 57 d) and Gl 581 (P = 130 d) (Fig. 1), but probably within the dispersion of the period-activity relation. The period closely matches that found in the RV residuals, reinforcing activity as an explanation for them.

To evaluate the stability of the 14 d signal, we split the RVs into four seasons (BJD–2 400 000 = 54 800–55 000, 55 400–55 600, 55 800–56 050, 56 150–56300; 25, 32, 43, 32 measurements per epoch) and computed periodograms for each. The 14 d is consistently present in every periodogram.

6. Radial velocities of GJ 3543

We obtained 80 RV measurements of GJ 3543 spanning 1919 d, with a dispersion σ_e = 3.02 m s^{-1} compared to an average photon noise combined with instrumental error of $\langle\sigma_i\rangle$ = 1.21 m s^{-1}. An F-test and a χ^2 test for a constant model find a $P < 10^{-9}$ probability that these known measurement errors explain the dispersion. The periodogram (Fig. 10) of the GJ 3543 RVs exhibits two strong peaks with powers of 0.37 and 0.34 at 1.1 and 9.2 d. Both peaks are well above the p = 0.29 for power at 0.3% FAP confidence level.

Our first *yorbit* one-Keplerian fit to the RVs converged on an orbit with period P = 1.11913 ± 0.00006, eccentricity e = 0.13 ± 0.16, and semi-amplitude K_1 = 2.70 ± 0.38 (2.6 ± 0.4 $M_\oplus$). This solution decreases the dispersion to σ_e = 2.32 m s^{-1} and the reduced χ^2 of the residuals to χ^2 = 3.80 ± 0.32. The 9.2 d signal disappears in the periodogram of the residuals, demonstrating that the 1.1 and 9.2 d peaks are aliases of each other. If we introduce a prior that mildly favors a longer period, the fit instead converges on an orbit with period P = 9.161 ± 0.004,

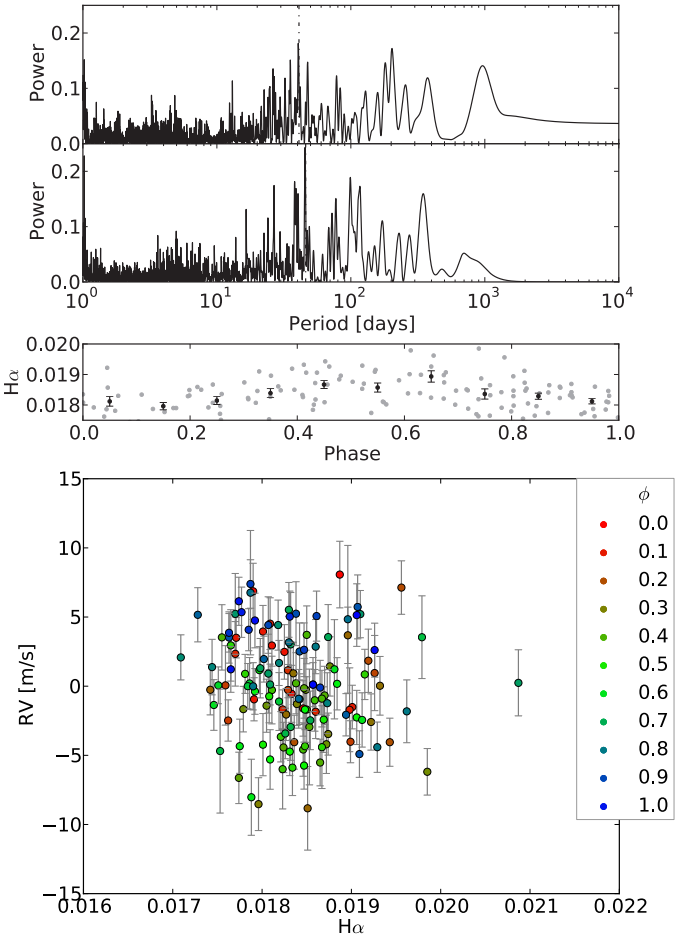

Fig. 9. *Top*: periodogram of the Hα emission index for GJ 3341, with a peak above the 3σ confidence level (continuous line) at 46 d. *Middle*: the Hα emission index phased to 46 d, which may represent the rotation period. *Bottom*: RV against Hα index, with colors representing the phase for the 14 d signal as in Fig. 8, T_0 from Table 5.

eccentricity e = 0.20±0.15, and semi-amplitude K_1 = 2.73±0.44 (5.1±0.9 $M_\oplus$), and the 1.1 d signal disappears in the periodogram of the residuals. Their dispersion is σ_e = 2.42 m s^{-1}, and the reduced χ^2 is χ^2 = 4.14 ± 0.33. In either case the strongest peak in the periodogram of the residuals occurs at 23 d and has a power p = 0.25, which corresponds to a ~2.5% FAP. The daily sampling of the observations and the periodogram analysis both suggest that the 1.1 and 9.2 d signals are aliases of one other (1/1.119 + 1/9.161 = 1/1.003). The residuals of the two fits do not differ enough to ascertain which represents the true signal, and Fig. 11 therefore plots both solutions.

6.1. Stellar activity

The power in the strongest peak in the periodogram of the S-index, (Fig. 12, second row), at 22 d, is p = 0.193 and just below the p = 0.198 needed for the 1σ confidence level. The strongest peak in the periodogram of the Hα index (Fig. 12, third row), at 19 d, is above the 1σ confidence level but still has a 14% FAP. Either period would be consistent with the strength of the Ca II emission line (Fig. 1), which suggest a stellar rotation period shorter than 35 d. While both activity signals have low significance, the P = 9.2 d radial velocity period is close the first harmonic of either 19 or 22 d, and the tentative 23 d peak in the periodogram of the RV residuals (Fig. 12, first row) is also

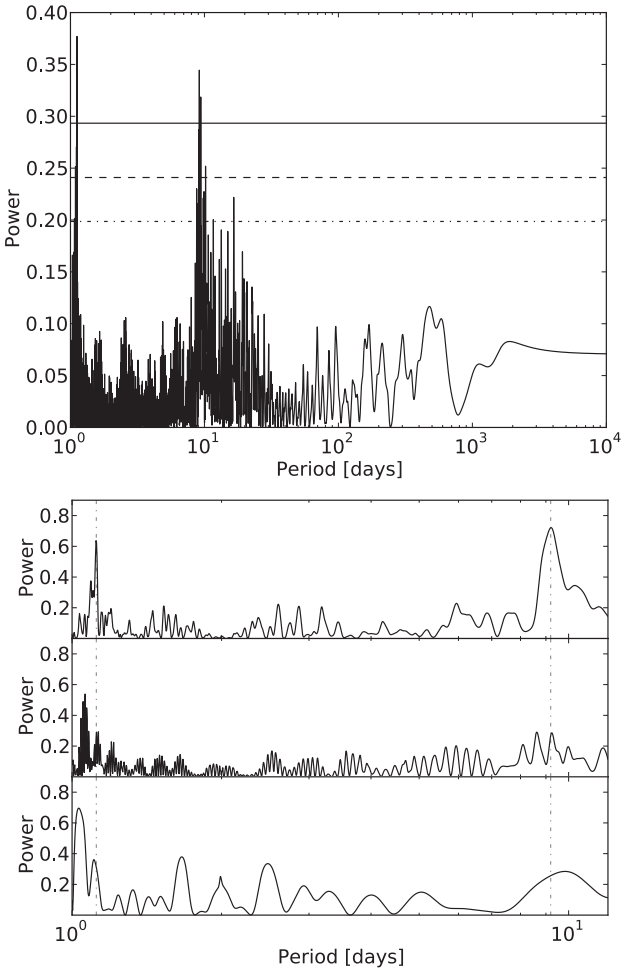

Fig. 10. *Top panel*: periodogram of the radial velocities of GJ 3543. The horizontal lines represent the same false-alarm levels as in Fig. 2. The two peaks at 1.1 and 9.2 d have an FAP lower than 0.3%. *Bottom panel*: periodograms for three independent subsets of observation epochs (BJD–2 400 000 = 55 500–55 750, *first row*; 55 850–56 050, *second row*; 56 340–56 380, *third row*). The 1.1 and 9.2 d peaks (marked by vertical dash-dotted lines) are both unstable over time.

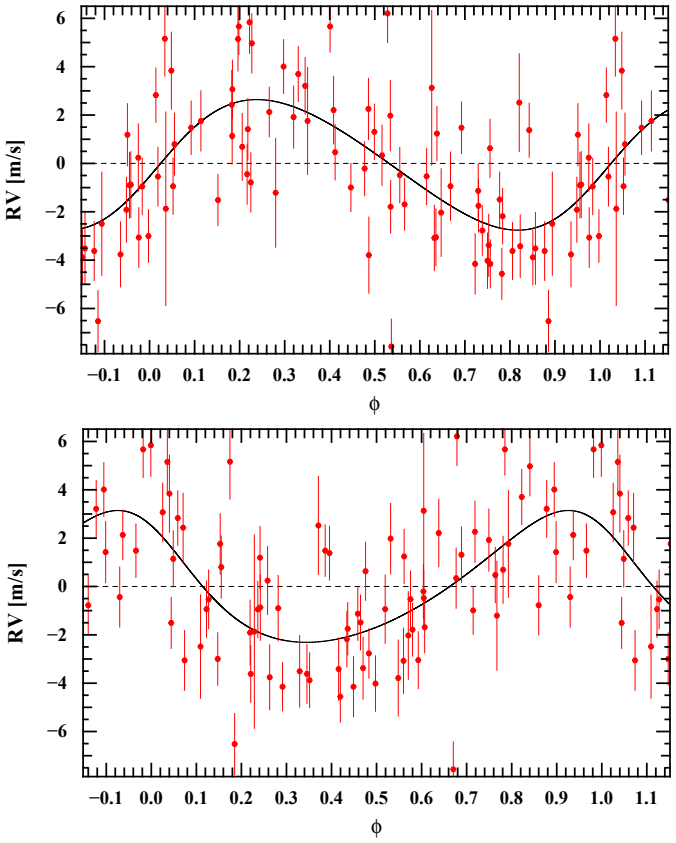

Fig. 11. Radials velocities for GJ 3543 RVs phased to the 1.1 d (*top*) and 9.2 d (*bottom*) period.

close to both. We evaluated the stability of the 1.1 or 9.2 d signal by computing periodograms for three disjoint seasons, BJD-2 400 000 = 55 500–55 750, 55 850–56 050, and 56 340–56 380, which contain 25, 30, and 14 measurements. The two aliased signals are only present in the first season and are absent from the second and third seasons (Fig. 10, bottom panel). The seasonal datasets have too few measurements for a similar exercise for the tentative 23 d peak in the periodogram of the residuals. Our best guess is that stellar activity is responsible for the RVs variation, although we see no correlation between the variations of the RV and of the S or Hα indices. More data are needed to ascertain the source of the RV dispersion.

The radial velocity signal at half the stellar rotation period found here for GJ 3543 has an analog in the recent reanalysis by Robertson et al. (2014) of the Forveille et al. (2011) GJ 581 data. This analogy provides an opportunity to summarize here the views of our team on the physical reality of the up to six planets that have been claimed to to orbit GJ 581, with heated controversies on the statistical significance of the weaker signals.

Our group announced the discoveries of "b" in 2005, followed by "c" and "d" in 2007 and then "e" in 2009 (Bonfils et al. 2005; Udry et al. 2007; Mayor et al. 2009), after considering both planetary and activity models in the interpretation of the observed periodic signals. The estimated rotational period of GJ 581 was much longer than the putative orbital periods of b, c and e, which consequently were immediately accepted as planets. The interpretation of the "d" signal was less straightforward because it occurred at a plausible rotational period for GJ 581. We discarded that explanation at the time, on the grounds that the Doppler variations, if caused by a spot on the rotating star, would have come together with larger photometric variations than observed (e.g., Bonfils et al. 2007). This made the planet the most likely interpretation, at that time.

Vogt et al. (2010) then combined the 2004 to 2008 HARPS data with new HIRES data, with most of the statistical weight on the HARPS side, to announce two additional planets in the system, f and g. We were monitoring GJ 581 very intensively, and we quickly reacted to the announcement of Vogt et al. (2010) by showing that our new HARPS data were incompatible with these additional two planets (Forveille et al. 2011). In that manuscript we relied on the measurement of Vogt et al. of a 90 d rotational period for GJ 581 to conclude that GJ 581d was a bona fide planet, since its period was comfortably away from any harmonic of the presumed rotational period.

Strong doubts, on different grounds, on the reality of GJ 581 f and g were also expressed by others (Tuomi 2011; Gregory 2011; Baluev 2013). Baluev et al. additionally questioned whether GJ 581d exists, finding that accounting for the correlated noise in the radial velocity measurements of GJ 581 decreased the significance of "d" to $\sim 1.5\sigma$. Robertson et al. more recently identified the astrophysical source of that correlated noise, showing that GJ 581 obeys a more complex RV-activity relation than previously thought. Instead of star spots, they

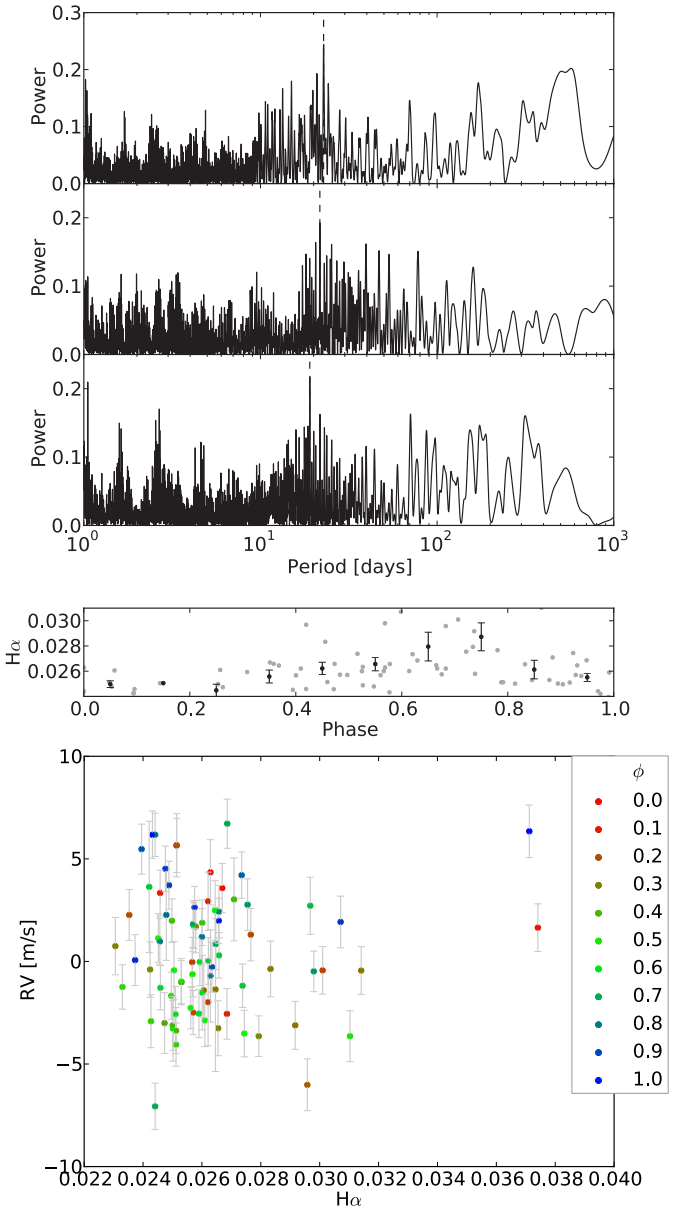

Fig. 12. *Top panel*: *first row*: periodogram of the residuals of the GJ 3543 radial velocities after subtracting the 1.1 d Keplerian orbit. The power excess at P = 23 d has a 2.5% FAP. *Second row*: periodogram of the S-index of GJ 3543. The significance of the 22 d peak is just under 1σ. *Third row*: periodogram of the Hα index of GJ 3543. The false-alarm probability of the 19 d peak is 14%. *Middle panel*: the Hα index phased to the 19 d period. *Bottom panel*: RVs against the Hα-index, the colors represent phase for the 9.2 d period, as represented in Fig. 11 (*bottom*), T_0 from Table 6.

invoked convection inhibition within active regions that locally changes the balance of ascending vs. descending material. Such active regions move as the star rotates and induce apparent Doppler shifts, but do not necessarily induce brightness variations. Robertson et al. additionally found the true rotation period of GJ 581 to be 130 days, quite different from that announced by Vogt et al. and twice the period of "d". These findings together mean that the 65 day radial velocity signal is most probably due to two longitudinally opposed active regions, and show that extra caution is warranted when RV periodicities are found near a harmonic of the rotation period. This occurs here for GJ 3543, and might also be the case for the GJ 667C system

Table 6. Fit for one-Keplerian of GJ 3543.

	GJ 3543(b)	GJ 3543(b)
P [d]	1.11913 ± 0.00006	9.161 ± 0.004
T_0 [JD–2 400 000]	55 739.52 ± 0.18	55 745.6 ± 1.0
ω [deg]	−100 ± 60	39.7 ± 43.3
e	0.13 ± 0.16	0.20 ± 0.15
K_1 [m s^{-1}]	2.70 ± 0.38	2.73 ± 0.44
$m \sin(i)$ [$M_\oplus$]	2.6 ± 0.4	5.1 ± 0.9
a [AU]	0 .0162	0.0657
γ [km s^{-1}]	15.0927 ± 0.0004	15.0932 ± 0.0005
$N_{\rm meas}$	80	80
Span [d]	1918.8	1918.8
$\langle\sigma_i\rangle$ [m s^{-1}]	1.21	1.21
σ_e [m s^{-1}]	2.32	2.42
χ^2_ν	3.80	4.14

(Delfosse et al. 2013a; Anglada-Escudé et al. 2013; Feroz & Hobson 2014), although its rotation period remains slightly uncertain.

7. Summary and conclusions

We analyzed observations of three early-M dwarfs with the HARPS spectrograph mounted on the 3.6 m telescope at La Silla observatory (ESO). We identified a planetary system orbiting GJ 3293, composed of two Neptunes with periods near the 4:1 resonance (30.6 ± 0.02 and 123.98 ± 0.38 d), and more tentatively a super-Earth with an orbital period of 48.14 ± 0.12 d. Although the RV variations appear to be uncorrelated with any stellar activity indicator, the orbital period of the least massive planet candidate remains moderately close to the plausible stellar rotation period. This signal is present and stable for the 2008−2009 and 2012−2013 subsets of the data, while the 2010−2011 subset has inadequate sampling to probe a 48 d period. More data are needed to fully confirm this planet candidate. With a 0.194 AU semi-major axis it orbits in the habitable zone of GJ 3293, and with a minimum mass of 7.9 ± 1.4 $M_\oplus$ it could be rocky. The hierarchical structure of the system warrants a dynamical analysis.

GJ 3341 is orbited by a super-Earth ($m \sin(i) \sim 6.6\ M_\oplus$) that is placed by its period of 14.207 ± 0.007 d in the inner habitable zone of its host star.

The periodogram of the radial velocities of GJ 3543 is dominated by two mutually aliased peaks at 1.1 and 9.2 d, but they are only present in a subset of the epochs. The periodograms of the stellar activity indices suggest a stellar rotation period of about 20 d, or approximately twice the 9.2 d period, which further reinforces the assumption that stellar activity is responsible for the unstable radial velocity signal – see Boisse et al. (2011).

GJ 3293 and GJ 3341 have approximately solar metallicity, consistently with the observation that the frequency of super-Earth and Neptune planets seems to be uncorrelated with stellar metallicity (Mayor et al. 2011; Sousa et al. 2011; Neves et al. 2013). As the sample of well-characterized planetary systems increases and stellar properties are more accurately known, we will refine the statistical relations between the presence of planets and the stellar properties of their hosts, which will help constrain planet formation and evolution models.

Acknowledgements. N.A. acknowledges support from CONICYT Becas-Chile 72120460. This publication makes use of data products from the Two Micron All Sky Survey, which is a joint project of the University of Massachusetts and the Infrared Processing and Analysis Center/California Institute of Technology, funded by the National Aeronautics and Space Administration and the National

Science Foundation. X.B., X.D., and T.F. acknowledge the support of the French Agence Nationale de la Recherche (ANR), under the program ANR-12-BS05-0012 Exo-atmos. X.B. acknowledges funding from the European Research Council under the ERC Grant Agreement No. 337591-ExTrA. N.C.S. acknowledges the support from the European Research Council/European Community under the FP7 through Starting Grant agreement number 239953. N.C.S. further acknowledges the support from Fundação para a Ciência e a Tecnologia (FCT, Portugal) through FEDER funds in program COMPETE, as well as through national funds, in the form of grants reference RECI/FIS-AST/0176/2012 (FCOMP-01-0124-FEDER-027493), and RECI/FIS-AST/0163/2012 (FCOMP-01-0124-FEDER-027492), and through the Investigador FCT contract reference IF/00169/2012 and POPH/FSE (EC) by FEDER funding through the program "Programa Operacional de Factores de Competitividade – COMPETE.

References

Anglada-Escudé, G., Tuomi, M., Gerlach, E., et al. 2013, A&A, 556, A126
Baluev, R. V. 2013, MNRAS, 429, 2052
Baranne, A., Queloz, D., Mayor, M., et al. 1996, A&AS, 119, 373
Boisse, I., Bouchy, F., Hébrard, G., et al. 2011, A&A, 528, A4
Bonfils, X., Forveille, T., Delfosse, X., et al. 2005, A&A, 443, L15
Bonfils, X., Mayor, M., Delfosse, X., et al. 2007, A&A, 474, 293
Bonfils, X., Delfosse, X., Udry, S., et al. 2013a, A&A, 549, A109
Bonfils, X., Lo Curto, G., Correia, A. C. M., et al. 2013b, A&A, 556, A110
Bouchy, F., Pepe, F., & Queloz, D. 2001, A&A, 374, 733
Boyajian, T. S., von Braun, K., van Belle, G., et al. 2012, ApJ, 757, 112
Cutri, R. M., Skrutskie, M. F., van Dyk, S., et al. 2003, VizieR Online Data Catalog, II/246
Delfosse, X., Forveille, T., Ségransan, D., et al. 2000, A&A, 364, 217
Delfosse, X., Bonfils, X., Forveille, T., et al. 2013a, A&A, 553, A8
Delfosse, X., Donati, J.-F., Kouach, D., et al. 2013b, in SF2A-2013: Proc. of the Annual Meet. of the French Society of Astronomy and Astrophysics, eds. L. Cambresy, F. Martins, E. Nuss, & A. Palacios, 497
Dressing, C. D., & Charbonneau, D. 2013, ApJ, 767, 95
Dumusque, X., Santos, N. C., Udry, S., Lovis, C., & Bonfils, X. 2011, A&A, 527, A82
Feroz, F., & Hobson, M. P. 2014, MNRAS, 437, 3540
Forveille, T., Bonfils, X., Delfosse, X., et al. 2011, unpublished [arXiv:1109.2505]
Fressin, F., Torres, G., Charbonneau, D., et al. 2013, ApJ, 766, 81
Gliese, W., & Jahreiß, H. 1991, Preliminary Version of the Third Catalogue of Nearby Stars, Tech. Rep.
Gomes da Silva, J., Santos, N. C., Bonfils, X., et al. 2011, A&A, 534, A30
Gregory, P. C. 2011, MNRAS, 415, 2523
Horne, J. H., & Baliunas, S. L. 1986, ApJ, 302, 757
Howarth, I. D., Siebert, K. W., Hussain, G. A. J., & Prinja, R. K. 1997, MNRAS, 284, 265
Johnson, D. R. H., & Soderblom, D. R. 1987, AJ, 93, 864
Kiraga, M., & Stepien, K. 2007, Acta Astron., 57, 149
Kürster, M., Endl, M., Rouesnel, F., et al. 2003, A&A, 403, 1077
Leggett, S. K. 1992, ApJS, 82, 351
Leggett, S. K., Allard, F., Geballe, T. R., Hauschildt, P. H., & Schweitzer, A. 2001, ApJ, 548, 908
Lovis, C., & Pepe, F. 2007, A&A, 468, 1115
Lucy, L. B. 2013, A&A, 551, A47
Mayor, M., Pepe, F., Queloz, D., et al. 2003, The Messenger, 114, 20
Mayor, M., Bonfils, X., Forveille, T., et al. 2009, A&A, 507, 487
Mayor, M., Marmier, M., Lovis, C., et al. 2011, A&A, submitted [arXiv:1109.2497]
Neves, V., Bonfils, X., Santos, N. C., et al. 2013, A&A, 551, A36
Neves, V., Bonfils, X., Santos, N. C., et al. 2014, A&A, 568, A121
Noyes, R. W., Hartmann, L. W., Baliunas, S. L., Duncan, D. K., & Vaughan, A. H. 1984, ApJ, 279, 763
Nutzman, P., & Charbonneau, D. 2008, PASP, 120, 317
Pepe, F., Mayor, M., Galland, F., et al. 2002, A&A, 388, 632
Queloz, D., Henry, G. W., Sivan, J. P., et al. 2001, A&A, 379, 279
Quintana, E. V., Barclay, T., Raymond, S. N., et al. 2014, Science, 344, 277
Quirrenbach, A., Amado, P. J., Seifert, W., et al. 2012, in SPIE Conf. Ser., 8446
Riedel, A. R., Subasavage, J. P., Finch, C. T., et al. 2010, AJ, 140, 897
Robertson, P., Mahadevan, S., Endl, M., & Roy, A. 2014, Science, 345, 440
Salim, S., & Gould, A. 2003, ApJ, 582, 1011
Selsis, F., Kasting, J. F., Levrard, B., et al. 2007, A&A, 476, 1373
Sousa, S. G., Santos, N. C., Israelian, G., Mayor, M., & Udry, S. 2011, A&A, 533, A141
Tuomi, M. 2011, A&A, 528, L5
Udry, S., Bonfils, X., Delfosse, X., et al. 2007, A&A, 469, L43
van Dokkum, P. G., & Conroy, C. 2010, Nature, 468, 940
Vidotto, A. A., Jardine, M., Morin, J., et al. 2013, A&A, 557, A67
Vogt, S. S., Butler, R. P., Rivera, E. J., et al. 2010, ApJ, 723, 954
Wheatley, P. J., Pollacco, D. L., Queloz, D., et al. 2013, in EPJ Web Conf., 47, 13002
Zacharias, N., Finch, C. T., Girard, T. M., et al. 2012, VizieR Online Data Catalog: I/322
Zechmeister, M., & Kürster, M. 2009, A&A, 496, 577
Zucker, S., & Mazeh, T. 2006, MNRAS, 371, 1513

Pages 12 to 19 are available in the electronic edition of the journal at http://www.aanda.org

Appendix A: RVs

The RVs are in the barycentric frame and are corrected for secular acceleration. The RVs were extracted through χ^2 matching to a template with a high S/N. The errors combine the estimated photon noise with the an estimate of the residual instrumental error (0.60 m s^{-1}). We also tabulate the FWHM and bisector span (BIS) of the CCF, as well as the activity indices of Hα and Ca II from Mount Wilson S.

Table A.1. GJ 3293 RVs, their uncertainty and activity indicators.

BJD – 2 400 000	RV [km s^{-1}]	σ_{RV} [km s^{-1}]	*FWHM* [km s^{-1}]	Contrast	BIS [km s^{-1}]	S-index	Hα
54 805.68424	13.28536	0.00375	3.60254	25.79888	–0.01715	1.42156	0.01814
54 825.64027	13.30846	0.00132	3.60782	25.14589	–0.00589	1.46394	0.02169
54 826.63445	13.31021	0.00146	3.60512	25.07722	–0.00330	1.33697	0.02091
54 827.64845	13.30529	0.00148	3.60866	24.69961	–0.01048	1.16751	0.02034
54 828.66060	13.30270	0.00176	3.59488	24.71040	–0.00372	1.42195	0.02112
54 829.76990	13.30312	0.00187	3.59572	25.10511	–0.01030	1.17184	0.02098
54 830.66322	13.29993	0.00168	3.60334	24.87551	–0.01416	1.20943	0.02054
54 831.65871	13.29726	0.00163	3.61586	24.87951	–0.01441	1.19192	0.02045
54 832.67287	13.29552	0.00265	3.60512	25.07722	–0.01191	1.28864	0.02036
54 833.66016	13.29525	0.00201	3.59258	24.73141	–0.00866	1.16719	0.02033
54 834.71626	13.29312	0.00151	3.60281	25.05025	–0.00988	1.28836	0.02150
54 848.62098	13.30394	0.00142	3.60453	24.78696	–0.01505	1.04256	0.01926
54 850.61453	13.30143	0.00163	3.60655	24.93891	–0.01737	1.00371	0.01937
54 852.63392	13.30466	0.00142	3.59689	25.03757	–0.00639	0.99302	0.01976
54 854.62660	13.30131	0.00169	3.58326	24.82394	–0.01598	1.16644	0.02056
54 879.59166	13.30268	0.00168	3.59159	25.00795	–0.00765	1.27681	0.01977
54 881.62441	13.29896	0.00193	3.62406	24.69537	–0.01938	1.28265	0.01991
54 883.52494	13.29997	0.00160	3.60304	24.86785	–0.01956	1.11932	0.01946
54 885.56408	13.29871	0.00169	3.61087	24.90341	–0.01129	1.31220	0.02157
55 045.92231	13.28938	0.00261	3.59152	24.95034	–0.00510	0.81714	0.02025
55 047.91349	13.28374	0.00247	3.59427	24.86074	–0.00797	1.37098	0.02086
55 049.92289	13.28389	0.00158	3.60506	24.76291	–0.01402	1.17482	0.01950
55 052.90367	13.28542	0.00152	3.59590	24.69413	–0.00863	1.18646	0.02269
55 121.83805	13.29732	0.00190	3.61108	25.01686	–0.02151	1.21001	0.02067
55 126.73175	13.29736	0.00163	3.60254	25.79888	–0.01083	1.42142	0.02057
55 129.71232	13.29868	0.00148	3.62406	24.69537	–0.00903	1.27998	0.02025
55 132.80321	13.29327	0.00165	3.60603	24.90897	–0.00752	1.21409	0.01984
55 135.70052	13.28911	0.00159	3.59773	24.87190	–0.00699	1.18975	0.02030
55 137.70695	13.28387	0.00136	3.60094	24.84526	–0.00258	1.18268	0.01970
55 139.73873	13.28154	0.00241	3.58700	25.11331	–0.01970	1.11593	0.01968
55 141.71517	13.28093	0.00179	3.60334	24.87551	–0.01763	1.04440	0.01961
55 143.68335	13.28173	0.00193	3.60264	24.91751	–0.01376	1.32279	0.02073
55 168.59826	13.28915	0.00157	3.59427	24.86074	–0.01506	1.23032	0.02106
55 169.62393	13.29108	0.00154	3.59996	25.14133	–0.00173	1.29228	0.02133
55 230.60800	13.29104	0.00190	3.61222	25.09914	–0.00660	1.31543	0.01965
55 403.92062	13.29672	0.00278	3.58700	25.11331	–0.00791	1.59816	0.02079
55 411.88037	13.29203	0.00522	3.59664	24.89766	0.010910	1.23556	0.01964
55 428.88535	13.30621	0.00220	3.59963	24.74944	–0.01358	1.44940	0.02034
55 437.86529	13.30170	0.00148	3.60730	25.03872	–0.01640	1.28391	0.02120
55 444.82380	13.29678	0.00165	3.61464	25.10732	–0.01627	1.19867	0.01971
55 450.88896	13.29711	0.00168	3.58700	25.11331	–0.00821	1.28313	0.02118
55 453.89333	13.29977	0.00172	3.59617	24.94721	–0.00742	1.14084	0.01986
55 454.82171	13.30149	0.00173	3.60655	24.93891	–0.00572	1.17555	0.01868
55 455.84630	13.30279	0.00240	3.60733	24.96234	0.003990	1.44517	0.02060
55 456.83313	13.29964	0.00158	3.60334	24.87551	–0.00749	1.16269	0.02018
55 457.86351	13.30165	0.00171	3.61401	24.96484	–0.01388	1.14233	0.02044
55 493.82107	13.30899	0.00183	3.60161	24.82933	–0.00736	1.01267	0.01915
55 494.76977	13.30460	0.00201	3.60531	24.80336	–0.01000	0.90454	0.01979
55 495.88051	13.30289	0.00147	3.60443	25.03226	–0.01423	1.15078	0.02096
55 497.75076	13.29815	0.00172	3.59634	24.89247	–0.01173	1.45566	0.01991
55 500.80695	13.29347	0.00177	3.59427	24.86074	–0.00835	1.08966	0.01979
55 501.75111	13.29021	0.00164	3.60512	25.07722	–0.00234	1.20944	0.01980
55 505.64461	13.28387	0.00192	3.61087	24.90341	–0.00057	1.05933	0.01954
55 514.68731	13.28270	0.00160	3.62495	25.00670	–0.00980	1.29677	0.02100

Table A.1. continued.

BJD – 2 400 000	RV [km s^{-1}]	σ_{RV} [km s^{-1}]	*FWHM* [km s^{-1}]	Contrast	BIS [km s^{-1}]	S-index	Hα
55 521.72610	13.29585	0.00176	3.59152	24.95034	–0.01461	0.99529	0.01948
55 523.71392	13.29791	0.00152	3.59773	24.87190	–0.01286	1.07141	0.01796
55 547.63328	13.29735	0.00161	3.60982	25.12058	–0.00594	1.25905	0.02011
55 548.59915	13.29992	0.00209	3.60418	24.92648	–0.00740	1.10584	0.01939
55 549.69948	13.30091	0.00146	3.59773	24.87190	–0.00374	1.26415	0.01951
55 576.59973	13.29605	0.00200	3.60971	24.95140	–0.01486	1.36858	0.02080
55 579.69290	13.30053	0.00174	3.60157	24.88640	–0.00178	1.26789	0.02069
55 586.57901	13.31199	0.00171	3.60418	24.92648	–0.00736	1.41550	0.02043
55 612.54944	13.30369	0.00163	3.60987	24.95725	–0.00820	0.95858	0.02007
55 615.50571	13.30480	0.00136	3.59152	24.95034	–0.01308	1.34022	0.02348
55 621.49969	13.29348	0.00155	3.61108	25.00144	–0.00568	1.04788	0.02114
55 817.89452	13.29597	0.00200	3.60593	24.70919	–0.00960	1.31675	0.02093
55 822.87888	13.30537	0.00148	3.59427	24.86074	–0.01346	1.08820	0.02093
55 825.89910	13.30804	0.00158	3.60626	24.86616	–0.01014	1.28318	0.02123
55 828.89202	13.30764	0.00148	3.61087	24.90341	–0.01200	1.21319	0.02042
55 829.85421	13.30775	0.00158	3.61053	24.63378	–0.01634	1.03953	0.01991
55 830.87234	13.30798	0.00174	3.61108	25.01686	–0.00494	1.05729	0.02050
55 831.83366	13.30569	0.00145	3.59617	24.94721	–0.01498	1.16617	0.02043
55 834.83622	13.30246	0.00178	3.60731	24.76752	–0.01487	0.90912	0.01919
55 835.76068	13.30133	0.00179	3.60731	24.76752	–0.00685	1.04509	0.01879
55 837.83127	13.30134	0.00134	3.61401	24.96484	–0.00813	0.99007	0.01913
55 839.82111	13.29755	0.00191	3.61053	24.63378	–0.00665	1.24796	0.01921
55 840.87205	13.29215	0.00154	3.60593	24.70919	–0.01234	1.15323	0.01961
55 841.75022	13.29021	0.00209	3.60443	25.03226	–0.00016	1.12326	0.01967
55 843.85888	13.28824	0.00153	3.63220	24.65556	–0.00897	1.15736	0.01989
55 870.76889	13.28400	0.00177	3.60512	25.07722	–0.00916	1.18192	0.02037
55 887.68502	13.29405	0.00264	3.60475	24.90774	–0.01196	1.31407	0.02025
55 890.67297	13.30346	0.00155	3.61108	25.00144	–0.00800	1.32079	0.02020
55 893.65958	13.30051	0.00181	3.60987	24.95725	–0.00797	1.33008	0.02026
55 924.64545	13.30390	0.00173	3.59588	24.67017	–0.00658	1.23348	0.01990
55 925.65007	13.30571	0.00170	3.59588	24.67017	–0.01338	1.05004	0.01901
55 926.63066	13.30337	0.00161	3.60593	24.70919	–0.00782	1.34434	0.02102
55 927.63859	13.30422	0.00199	3.59468	24.91635	–0.02377	1.13228	0.02013
55 928.68246	13.30283	0.00183	3.60414	24.99914	–0.01468	1.02394	0.01955
55 929.61470	13.30281	0.00182	3.59996	25.14133	–0.00695	1.06086	0.01966
55 930.63306	13.30300	0.00180	3.60094	24.84526	–0.01513	1.32293	0.02008
55 931.61582	13.30170	0.00194	3.60673	24.81264	–0.01145	0.95326	0.01945
55 932.61626	13.29942	0.00163	3.60836	25.01811	–0.01263	1.26315	0.01968
55 933.63090	13.30062	0.00164	3.60987	24.95725	–0.01078	1.28021	0.01986
55 940.55035	13.28895	0.00246	3.60512	25.07722	–0.01183	1.54123	0.02028
55 941.64214	13.29572	0.00152	3.60512	25.07722	–0.01156	1.34513	0.01968
55 942.69832	13.29324	0.00199	3.59387	24.89050	–0.00825	0.78451	0.01891
55 943.63946	13.29661	0.00209	3.59159	25.00795	–0.01181	1.39953	0.02046
55 944.63016	13.29985	0.00194	3.60512	25.07722	–0.00650	1.27652	0.01975
55 945.64138	13.29997	0.00175	3.60836	25.01811	–0.00485	1.12134	0.02054
55 946.63701	13.29891	0.00172	3.61087	24.90341	–0.00512	1.19637	0.02023
55 947.62134	13.29747	0.00162	3.60847	24.79972	–0.01226	1.11409	0.01987
55 949.61627	13.30076	0.00160	3.60593	24.70919	–0.00916	1.27358	0.01952
55 950.62808	13.30303	0.00170	3.59427	24.86074	0.002250	1.40957	0.02118
55 997.53126	13.27822	0.00210	3.59661	24.78567	–0.01016	1.19986	0.01991
56 001.48895	13.27508	0.00181	3.59152	24.95034	–0.01171	1.11461	0.01953
56 008.50764	13.28963	0.00166	3.60475	24.90774	–0.01240	0.91820	0.02015
56 010.51342	13.29753	0.00169	3.60687	24.94252	–0.01324	1.23211	0.01990
56 022.50593	13.29470	0.00233	3.60414	24.99914	–0.01226	1.26817	0.02117
56 025.48481	13.28588	0.00262	3.61057	24.94123	–0.00658	1.71769	0.02326
56 030.48582	13.27992	0.00314	3.62180	24.78081	–0.00097	1.08995	0.02079
56 032.47450	13.28219	0.00329	3.61087	24.90341	–0.00691	0.94920	0.02031
56 158.86499	13.29079	0.00207	3.61087	24.90341	–0.00884	1.01209	0.02149
56 160.88634	13.29507	0.00184	3.60945	24.54870	–0.01014	1.32960	0.02247
56 171.84600	13.30300	0.00173	3.61245	24.91672	–0.01102	1.04735	0.01955
56 208.85566	13.29100	0.00315	3.60161	24.82933	–0.02114	1.55485	0.02022
56 209.86400	13.28648	0.00395	3.60161	24.82933	0.005810	1.43810	0.01896
56 210.84941	13.29442	0.00188	3.61586	24.87951	–0.00965	1.14180	0.01895
56 221.86931	13.30292	0.00222	3.60731	24.76752	–0.02148	1.17186	0.02089
56 229.75711	13.30168	0.00175	3.60945	24.54870	–0.00017	1.20497	0.02203

Table A.1. continued.

BJD – 2 400 000	RV [km s^{-1}]	σ_{RV} [km s^{-1}]	*FWHM*	Contrast [km s^{-1}]	BIS [km s^{-1}]	S-index	Hα
56 230.70914	13.30124	0.00215	3.60945	24.54870	–0.01921	1.27728	0.02073
56 231.78090	13.29747	0.00171	3.60414	24.99914	–0.01103	1.22611	0.02255
56 235.66439	13.29494	0.00245	3.60094	24.84526	–0.01364	1.24985	0.02070
56 236.65314	13.29105	0.00225	3.60161	24.82933	–0.00832	1.19125	0.02073
56 237.64360	13.28785	0.00194	3.60687	24.94252	–0.00697	0.99914	0.01952
56 238.61253	13.28867	0.00191	3.61290	24.88298	–0.00562	1.03800	0.02031
56 239.66651	13.28278	0.00229	3.59152	24.95034	–0.01184	1.39054	0.02107
56 245.61339	13.28206	0.00229	3.60094	24.84526	–0.01789	1.08137	0.02135
56 248.64851	13.28634	0.00250	3.59152	24.95034	–0.01662	1.04436	0.01965
56 249.67253	13.28603	0.00203	3.61977	24.86813	–0.00928	1.04205	0.01879
56 251.69011	13.29099	0.00164	3.61977	24.86813	–0.01375	0.97448	0.01930
56 252.65403	13.29243	0.00161	3.59427	24.86074	–0.01224	0.90649	0.02016
56 253.65586	13.29557	0.00207	3.61057	24.94123	–0.01020	1.04962	0.01978
56 256.68998	13.30221	0.00199	3.61028	25.10494	–0.01632	0.91982	0.01981
56 257.72995	13.29963	0.00168	3.59427	24.86074	–0.00962	1.14657	0.02025
56 259.64344	13.30642	0.00194	3.59427	24.86074	–0.01992	1.25647	0.01963
56 263.63688	13.30049	0.00252	3.61977	24.86813	–0.01724	1.26143	0.02204
56 264.78151	13.29736	0.00144	3.61057	24.94123	–0.01889	1.41208	0.02171
56 283.56533	13.29611	0.00203	3.60761	24.95206	–0.02231	1.07310	0.02025
56 304.65270	13.29140	0.00186	3.61977	24.86813	–0.00839	1.22813	0.02022
56 307.60791	13.29589	0.00154	3.60660	24.80012	–0.01032	1.22408	0.02136
56 312.60633	13.30676	0.00191	3.60660	24.80012	–0.01124	1.24584	0.02156
56 314.60875	13.30923	0.00197	3.60660	24.80012	–0.01178	1.19865	0.02082
56 316.64222	13.31724	0.00210	3.60687	24.94252	–0.01251	0.84569	0.02116
56 318.64452	13.31640	0.00228	3.59152	24.95034	0.001300	1.25696	0.02065
56 319.65567	13.31447	0.00249	3.59152	24.95034	–0.01262	1.13835	0.02063

Table A.2. GJ 3341 RVs, its uncertainty and activity indicators.

BJD – 2 400 000	RV [km s^{-1}]	σ_{RV} [km s^{-1}]	*FWHM* [km s^{-1}]	Contrast	BIS [km s^{-1}]	S-index	Hα
54 807.69849	47.79778	0.00448	3.59435	25.43663	–0.00157	0.26432	0.01753
54 825.66746	47.80633	0.00139	3.59007	24.79779	–0.01287	0.98919	0.01763
54 826.64838	47.80369	0.00166	3.59320	24.70898	–0.01375	0.94571	0.01765
54 827.66095	47.80152	0.00156	3.58260	24.76051	–0.01041	0.98700	0.01791
54 828.67307	47.80220	0.00184	3.60239	24.53064	–0.00977	0.95732	0.01829
54 829.78186	47.80221	0.00182	3.59904	24.80998	–0.00928	1.06308	0.01742
54 830.65130	47.79394	0.00191	3.60239	24.53064	–0.01033	0.80047	0.01796
54 831.64673	47.79584	0.00186	3.60781	24.79868	–0.00639	0.86513	0.01774
54 832.65658	47.79647	0.00288	3.61297	24.63142	–0.01826	0.95837	0.01823
54 833.64792	47.80005	0.00237	3.58617	24.68657	0.004100	0.98841	0.01869
54 834.77493	47.79813	0.00196	3.58447	24.62698	–0.00381	0.89096	0.01775
54 849.56753	47.80253	0.00133	3.60043	24.95740	–0.01658	0.76761	0.01751
54 851.62802	47.80455	0.00163	3.59861	24.84315	–0.00214	0.86549	0.01709
54 881.63742	47.80599	0.00185	3.60168	24.77744	–0.01260	0.88508	0.01763
54 882.59568	47.80655	0.00152	3.57915	24.67109	–0.00921	0.87898	0.01785
54 885.54247	47.79999	0.00149	3.59581	24.69552	–0.01145	0.72763	0.01762
54 932.48536	47.80336	0.00141	3.59952	24.69259	–0.00620	0.98036	0.01781
54 934.48545	47.80111	0.00183	3.57877	24.88057	–0.00601	0.93246	0.01746
54 937.48457	47.80246	0.00171	3.59007	24.79779	–0.01399	0.71549	0.01790
54 940.49248	47.80722	0.00198	3.59435	25.43663	–0.01607	0.75937	0.01792
54 941.48780	47.80597	0.00146	3.59595	24.58150	–0.01188	0.78320	0.01771
54 949.46243	47.80247	0.00164	3.60630	24.90630	–0.00476	0.89015	0.01784
54 950.46139	47.80259	0.00148	3.60283	24.58144	–0.01222	0.83795	0.01809
54 954.46978	47.80861	0.00174	3.58580	24.60535	–0.01058	0.52661	0.01774
54 955.46854	47.80541	0.00149	3.58382	24.68647	0.002070	0.93699	0.01811
55 220.56224	47.80338	0.00285	3.61297	24.63142	–0.01453	0.81790	0.01807
55 225.54498	47.80642	0.00189	3.57878	24.65019	–0.01519	0.78821	0.01801
55 229.69119	47.79952	0.00419	3.59055	24.71588	–0.01973	1.01882	0.01853
55 423.91008	47.81054	0.00241	3.60986	24.65434	–0.00866	0.73691	0.01887
55 425.90482	47.80960	0.00193	3.59595	24.58150	–0.01869	0.97592	0.01956
55 427.92239	47.80106	0.00192	3.60196	24.58954	–0.01762	1.00509	0.01805
55 428.90390	47.80268	0.00221	3.60507	24.73606	–0.02268	0.72720	0.01838
55 434.88752	47.80564	0.00188	3.60725	24.58705	–0.00987	0.89913	0.01830
55 437.84917	47.80258	0.00159	3.58580	24.60535	–0.01455	0.79242	0.01857
55 444.85801	47.79774	0.00174	3.58447	24.62698	–0.00217	0.79058	0.01831
55 480.81601	47.80086	0.00200	3.59904	24.80998	–0.00349	0.35148	0.01846
55 483.80314	47.79988	0.00203	3.59435	25.43663	–0.00897	0.86845	0.01922
55 486.76213	47.79658	0.00202	3.61114	24.58479	–0.02042	0.86073	0.01834
55 492.87155	47.80689	0.00204	3.60507	24.73606	–0.01635	0.23161	0.01807
55 495.89290	47.80079	0.00141	3.57375	25.51735	–0.00911	0.45954	0.01823
55 497.80927	47.80042	0.00188	3.59822	24.88792	–0.00811	0.62883	0.01827
55 499.87347	47.80078	0.00237	3.60630	24.90630	–0.01653	0.57420	0.01850
55 501.81020	47.80021	0.00196	3.58758	24.75806	–0.01099	0.39399	0.01906
55 505.70282	47.79806	0.00182	3.61193	24.76277	–0.01927	0.33693	0.01929
55 506.78000	47.79756	0.00168	3.59007	24.79779	–0.01096	0.64716	0.01909
55 509.76158	47.80096	0.00158	3.58447	24.62698	–0.00909	0.77938	0.01901
55 510.73594	47.79845	0.00152	3.58758	24.75806	–0.01222	0.64301	0.01899
55 512.72825	47.79901	0.00152	3.61448	24.53406	–0.00851	0.69542	0.01874
55 513.74985	47.80232	0.00216	3.60000	24.56756	–0.00294	0.71029	0.01847
55 514.75421	47.79813	0.00163	3.61448	24.53406	–0.01779	0.72800	0.01848
55 518.69233	47.80377	0.00215	3.60202	24.58428	–0.00779	0.85978	0.01798
55 519.63904	47.80124	0.00220	3.58447	24.62698	–0.00783	0.77323	0.01873
55 521.74963	47.80237	0.00197	3.60000	24.56756	–0.00606	0.67096	0.01865
55 522.70507	47.80259	0.00195	3.60158	24.22742	–0.01546	0.74732	0.01857
55 523.75227	47.80495	0.00197	3.58240	24.93187	–0.00250	0.80502	0.01825
55 539.63328	47.79842	0.00195	3.59768	24.61102	–0.01136	0.57500	0.01836
55 542.69632	47.79789	0.00193	3.59055	24.71588	–0.01205	0.73343	0.01846
55 544.69892	47.80078	0.00146	3.61297	24.63142	–0.00999	0.64341	0.01848
55 546.60740	47.79905	0.00183	3.58382	24.68647	–0.01044	0.83876	0.01826
55 547.68313	47.80689	0.00181	3.61073	24.59018	–0.01538	0.71074	0.01818
55 817.91683	47.80415	0.00163	3.58758	24.75806	–0.01648	0.69149	0.01819
55 871.72296	47.80264	0.00189	3.56078	24.55298	–0.00979	0.76060	0.01884
55 875.75986	47.80443	0.00166	3.60406	24.82217	–0.01232	0.78623	0.01802
55 887.80195	47.80000	0.00212	3.59476	24.55047	–0.00840	0.83975	0.01854
55 889.67389	47.80156	0.00212	3.59822	24.88792	–0.02224	0.85840	0.01841

Table A.2. continued.

BJD – 2 400 000	RV [km s^{-1}]	σ_{RV} [km s^{-1}]	*FWHM* [km s^{-1}]	Contrast	BIS [km s^{-1}]	S-index	Hα
55 891.67563	47.80750	0.00185	3.61297	24.63142	–0.01742	0.53778	0.01831
55 893.67046	47.80062	0.00194	3.58916	24.51550	–0.01489	0.63131	0.01860
55 895.71856	47.80340	0.00225	3.56078	24.55298	–0.00774	0.95793	0.01835
55 924.65743	47.80118	0.00156	3.62850	24.25183	–0.01020	0.60524	0.01839
55 925.60322	47.79804	0.00182	3.59435	25.43663	–0.01511	1.38852	0.01824
55 926.68814	47.79881	0.00182	3.59476	24.55047	–0.00395	0.63496	0.01821
55 927.67658	47.79824	0.00225	3.59061	24.89397	–0.01865	0.93117	0.01801
55 928.78900	47.79444	0.00275	3.62850	24.25183	–0.01484	0.38422	0.01788
55 929.67904	47.80136	0.00209	3.59492	24.50066	–0.01258	0.69748	0.01819
55 930.68755	47.80549	0.00375	3.59861	24.84315	–0.01588	0.89780	0.01832
55 931.63830	47.80153	0.00183	3.59435	25.43663	–0.00241	0.73302	0.01842
55 932.66330	47.80040	0.00153	3.59597	24.72643	–0.01358	0.67666	0.01894
55 933.70230	47.80510	0.00194	3.59435	25.43663	–0.01285	0.69418	0.01847
55 940.66160	47.80219	0.00245	3.60240	24.72910	0.001540	0.65311	0.01811
55 941.73303	47.80174	0.00192	3.60202	24.58428	–0.00592	0.53807	0.01808
55 942.65135	47.80209	0.00165	3.58580	24.60535	–0.00790	0.83814	0.01792
55 943.74352	47.80267	0.00187	3.60196	24.58954	–0.01134	0.89701	0.01786
55 944.74860	47.80799	0.00198	3.57878	24.65019	–0.00388	0.88405	0.01830
55 945.74749	47.80385	0.00201	3.59861	24.84315	–0.01403	1.17721	0.01744
55 946.74356	47.80763	0.00196	3.61448	24.53406	–0.00446	0.48098	0.01728
55 947.72814	47.80986	0.00175	3.60507	24.73606	–0.01318	0.47686	0.01787
55 948.72736	47.80782	0.00182	3.59435	25.43663	–0.01832	0.67393	0.01777
55 949.72113	47.80933	0.00203	3.60071	24.82345	–0.02080	0.70198	0.01790
55 950.73282	47.80362	0.00199	3.59822	24.88792	–0.01702	0.89344	0.01829
55 997.54782	47.80145	0.00223	3.59899	24.73087	–0.01361	0.77080	0.01859
55 999.50620	47.80363	0.00170	3.60071	24.82345	–0.01048	0.99767	0.01797
56 001.57468	47.80602	0.00235	3.59061	24.89397	–0.01014	1.01487	0.01874
56 004.48819	47.80754	0.00181	3.58120	24.91090	–0.01921	0.81673	0.01861
56 006.56154	47.80192	0.00206	3.60283	24.58144	–0.01552	0.85736	0.01833
56 008.52020	47.79842	0.00174	3.60406	24.82217	–0.00322	0.95240	0.01943
56 013.54468	47.79717	0.00215	3.59818	24.55765	–0.00810	0.98921	0.01809
56 021.50098	47.80481	0.00233	3.60196	24.58954	–0.00390	0.78758	0.01770
56 024.48555	47.80081	0.00165	3.58729	24.69291	–0.01661	0.49211	0.01779
56 025.49723	47.80600	0.00236	3.59492	24.50066	–0.02052	1.52699	0.01755
56 026.50327	47.80542	0.00258	3.57878	24.65019	–0.00644	0.65928	0.01765
56 029.52945	47.79952	0.00241	3.58729	24.69291	–0.01481	0.43675	0.01832
56 030.51172	47.80770	0.00292	3.58758	24.75806	0.009850	0.35110	0.01770
56 031.51835	47.80923	0.00450	3.59858	24.52790	–0.05071	0.37144	0.01787
56 180.85874	47.80221	0.00287	3.60353	24.35406	–0.01243	0.91964	0.01849
56 181.87228	47.80618	0.00209	3.60071	24.82345	–0.01439	1.07214	0.01850
56 182.87143	47.79806	0.00299	3.58335	24.87303	–0.00710	0.36638	0.01867
56 186.84912	47.80768	0.00171	3.59858	24.52790	–0.01119	1.00343	0.01910
56 187.86191	47.80731	0.00534	3.59861	24.84315	0.001580	1.51751	0.01896
56 190.88488	47.80761	0.00226	3.59858	24.52790	0.002050	0.85908	0.01906
56 192.86732	47.80342	0.00272	3.59595	24.58150	–0.00316	0.88605	0.01926
56 193.85343	47.80615	0.00204	3.59822	24.88792	–0.01101	1.09271	0.01896
56 194.87392	47.80390	0.00214	3.59061	24.89397	–0.00833	0.69008	0.01876
56 195.83731	47.80180	0.00211	3.58335	24.87303	–0.00925	0.79571	0.01870
56 196.84078	47.80332	0.00182	3.60071	24.82345	–0.00746	0.93673	0.01915
56 198.85435	47.80369	0.00359	3.61448	24.53406	–0.01265	0.03357	0.01881
56 199.85744	47.80601	0.00299	3.60353	24.35406	–0.01251	0.48219	0.01979
56 200.82093	47.80271	0.00239	3.61448	24.53406	–0.02950	0.95819	0.02087
56 201.82289	47.80065	0.00227	3.57375	25.51735	–0.00588	1.16869	0.01962
56 202.87283	47.80820	0.00231	3.59299	24.63871	–0.01651	0.92122	0.01907
56 235.67528	47.80431	0.00229	3.61565	24.52854	–0.01613	0.67675	0.01919
56 236.68649	47.80250	0.00212	3.60071	24.82345	–0.01686	1.06575	0.01932
56 237.65447	47.79827	0.00211	3.61565	24.52854	–0.00715	0.80598	0.01872
56 238.71167	47.80157	0.00205	3.59299	24.63871	–0.01038	0.84328	0.01867
56 245.62430	47.80771	0.00231	3.59858	24.52790	–0.01033	1.22042	0.01838
56 247.61995	47.80508	0.00195	3.59858	24.52790	–0.01245	0.41762	0.01926
56 248.70192	47.80076	0.00303	3.61222	24.92663	–0.01091	0.72502	0.01898
56 250.65160	47.79364	0.00302	3.58479	24.64203	–0.00648	0.69128	0.01851
56 251.70851	47.79628	0.00168	3.60071	24.82345	–0.01358	0.98762	0.01985
56 252.66497	47.79695	0.00169	3.59861	24.84315	–0.00728	0.91803	0.01865
56 254.67894	47.79673	0.00170	3.60071	24.82345	–0.01269	0.90922	0.01847
56 255.61817	47.80003	0.00196	3.59861	24.84315	–0.01083	0.85057	0.01912

Table A.2. continued.

BJD – 2 400 000	RV [km s^{-1}]	σ_{RV} [km s^{-1}]	*FWHM* [km s^{-1}]	Contrast	BIS [km s^{-1}]	S-index	Hα
56 258.65243	47.80533	0.00196	3.61222	24.92663	–0.01172	0.99596	0.01860
56 259.65469	47.80498	0.00206	3.59858	24.52790	–0.01031	0.71719	0.01842
56 262.81151	47.80699	0.00187	3.61222	24.92663	–0.00262	0.97329	0.01809
56 263.64804	47.80253	0.00287	3.59861	24.84315	0.001800	0.60908	0.01759

Table A.3. GJ 3543 RVs, its uncertainty and activity indicators.

BJD – 2 400 000	RV [km s^{-1}]	σ_{RV} [km s^{-1}]	*FWHM* [km s^{-1}]	Contrast	BIS [km s^{-1}]	S-index	Hα
54 455.81748	15.09084	0.00134	3.72672	20.74941	–0.00725	2.42133	0.02606
54 825.82158	15.09106	0.00106	3.72954	20.77381	–0.01019	2.56120	0.02738
54 826.80721	15.09176	0.00099	3.72600	20.51434	–0.01092	2.81219	0.02980
54 827.79556	15.09645	0.00113	3.72417	20.60870	–0.01565	2.50082	0.02735
54 828.84278	15.09488	0.00102	3.72244	20.63083	–0.00892	2.44846	0.02575
54 829.86968	15.09389	0.00116	3.72703	20.57069	–0.01032	3.22177	0.03741
54 830.84558	15.09355	0.00128	3.72672	20.74941	–0.00975	2.52963	0.02766
54 831.83059	15.08899	0.00134	3.74139	20.73712	–0.01837	2.36949	0.02655
54 832.82130	15.09527	0.00202	3.72834	20.68230	–0.01583	2.49733	0.02709
54 833.84856	15.08998	0.00102	3.72406	20.60702	–0.01285	2.34166	0.02562
54 834.85241	15.08970	0.00117	3.72600	20.51434	–0.01553	2.34512	0.02590
55 585.79129	15.09399	0.00112	3.73041	20.77120	–0.00931	2.31790	0.02572
55 589.80228	15.09859	0.00128	3.72267	20.56052	–0.01017	3.38598	0.03712
55 593.78829	15.09057	0.00114	3.72497	20.54240	–0.01024	2.32222	0.02496
55 622.60745	15.09096	0.00108	3.71482	20.57990	–0.01538	2.38990	0.02459
55 628.66836	15.09394	0.00128	3.72876	20.54426	–0.01323	2.43931	0.02579
55 629.67559	15.08887	0.00113	3.72244	20.63083	–0.00841	2.38816	0.02512
55 630.71219	15.09126	0.00113	3.72556	20.54603	–0.00792	2.26502	0.02530
55 632.67210	15.09896	0.00120	3.73159	20.72365	–0.01588	2.48187	0.02686
55 633.64839	15.09842	0.00106	3.72956	20.71123	–0.01093	2.22836	0.02441
55 634.65201	15.09676	0.00111	3.73331	20.43016	–0.01097	2.21318	0.02476
55 638.63504	15.08924	0.00148	3.72343	20.56211	–0.00809	2.33684	0.02473
55 639.61274	15.09100	0.00108	3.72834	20.68230	–0.00523	2.07769	0.02330
55 642.61391	15.09322	0.00114	3.72020	20.23990	–0.00761	2.28483	0.02457
55 643.65849	15.09596	0.00117	3.72889	20.73374	–0.01364	2.40455	0.02488
55 644.61310	15.09842	0.00116	3.72672	20.74941	–0.01466	2.29391	0.02432
55 648.62383	15.08819	0.00105	3.73091	20.59071	–0.01140	2.31546	0.02512
55 652.47921	15.09772	0.00122	3.73159	20.72365	–0.01962	2.10686	0.02395
55 654.47899	15.09558	0.00112	3.73555	20.57637	–0.00779	2.20247	0.02458
55 657.47653	15.09423	0.00106	3.73033	20.64375	–0.01483	2.19046	0.02498
55 659.47423	15.09254	0.00111	3.72149	20.50567	–0.01244	2.39384	0.02658
55 663.47053	15.09659	0.00159	3.73030	20.62977	–0.01156	2.30264	0.02629
55 672.58915	15.09790	0.00132	3.72621	20.59418	–0.00882	2.40820	0.02514
55 676.56936	15.08937	0.00128	3.72149	20.50567	–0.01097	2.46696	0.02610
55 677.53431	15.09222	0.00116	3.72684	20.52647	–0.01197	2.42020	0.02593
55 711.48912	15.09185	0.00135	3.72591	20.59257	–0.00970	2.20280	0.02424
55 871.80485	15.09344	0.00138	3.72668	20.74823	–0.01336	2.40549	0.02600
55 874.81344	15.09026	0.00213	3.72822	20.66578	–0.01024	1.82523	0.02621
55 875.83369	15.08913	0.00117	3.72700	20.55149	–0.01043	2.49935	0.02917
55 878.83418	15.08896	0.00157	3.73700	20.74596	–0.00988	1.98883	0.02502
55 880.84096	15.09154	0.00225	3.73700	20.74596	–0.00593	1.89586	0.02629
55 887.84060	15.09473	0.00145	3.72962	20.59683	–0.00095	2.11055	0.02645
55 888.81874	15.09496	0.00139	3.72538	20.63755	–0.02545	2.28485	0.02968
55 889.83853	15.09467	0.00128	3.72729	20.55800	–0.01148	2.24282	0.02658
55 890.85136	15.09197	0.00122	3.72556	20.54603	–0.01304	2.23126	0.02634
55 891.82222	15.09423	0.00110	3.72834	20.68230	–0.00681	2.22775	0.02657
55 892.81128	15.08969	0.00123	3.73033	20.64375	–0.01456	2.19169	0.02685
55 893.82921	15.08623	0.00126	3.72497	20.54240	–0.00686	2.63181	0.02958
55 894.80379	15.08860	0.00099	3.71482	20.57990	–0.01143	2.44420	0.02793
55 996.71895	15.08933	0.00129	3.72834	20.68230	–0.01343	2.20589	0.02427
55 997.66483	15.09181	0.00141	3.72429	20.76135	–0.01131	2.00610	0.02505
56 002.71704	15.09518	0.00142	3.72385	20.47525	–0.00842	2.51458	0.02621
56 003.66997	15.09791	0.00154	3.72703	20.57069	–0.01109	2.11422	0.02514
56 005.69427	15.09413	0.00111	3.72385	20.47525	–0.00943	2.22501	0.02601
56 007.61106	15.09227	0.00114	3.72834	20.68230	–0.01083	2.16732	0.02622
56 008.65231	15.09501	0.00126	3.72406	20.60702	–0.01046	2.43808	0.02755
56 010.58917	15.09231	0.00124	3.71482	20.57990	–0.01457	2.09934	0.02373
56 011.63581	15.09124	0.00105	3.72834	20.68230	–0.00894	2.21262	0.02530
56 012.58228	15.08975	0.00108	3.72668	20.74823	–0.00738	2.13713	0.02570
56 020.62473	15.09582	0.00120	3.72889	20.73374	–0.01451	2.35845	0.02669
56 021.55890	15.09221	0.00121	3.72874	20.80548	–0.01195	2.20731	0.02567
56 022.61059	15.09188	0.00136	3.72429	20.76135	–0.01761	2.29623	0.02833
56 024.59278	15.09162	0.00110	3.72729	20.55800	–0.00916	2.19298	0.02568
56 025.61982	15.09072	0.00181	3.72729	20.55800	–0.01316	2.05005	0.02601
56 026.59209	15.09309	0.00124	3.72874	20.55294	–0.01012	2.54414	0.02647

Table A.3. continued.

BJD – 2 400 000	RV [km s^{-1}]	σ_{RV} [km s^{-1}]	*FWHM* [km s^{-1}]	Contrast	BIS [km s^{-1}]	S-index	Hα
56 031.65055	15.09088	0.00400	3.71807	20.53797	–0.00700	0.88335	0.02646
56 354.75925	15.08873	0.00114	3.72874	20.80548	–0.01113	2.28217	0.02744
56 355.73982	15.09588	0.00320	3.72516	20.45809	–0.01596	0.79015	0.02421
56 360.76207	15.09451	0.00124	3.73555	20.57637	–0.00976	2.18953	0.02353
56 361.72566	15.09299	0.00140	3.71807	20.53797	–0.01023	1.86769	0.02306
56 363.71853	15.09338	0.00120	3.72889	20.73374	–0.00886	2.04838	0.02452
56 365.66954	15.09406	0.00114	3.72889	20.73374	–0.01144	2.21021	0.02570
56 366.62280	15.09451	0.00221	3.72149	20.50567	–0.02034	2.23726	0.02479
56 367.59345	15.09417	0.00126	3.71482	20.57990	–0.01291	3.05196	0.03071
56 369.64591	15.09181	0.00116	3.72874	20.55294	–0.00923	2.62690	0.03010
56 370.68844	15.09180	0.00116	3.72149	20.50567	–0.00527	3.07099	0.03141
56 371.68821	15.08913	0.00121	3.72149	20.50567	–0.01343	2.26730	0.02501
56 372.63459	15.08860	0.00124	3.75693	20.44840	–0.01294	2.76210	0.03103
56 373.65240	15.08967	0.00135	3.72874	20.80548	–0.01542	2.24918	0.02510
56 374.66466	15.08518	0.00113	3.72149	20.50567	–0.00944	2.12089	0.02441